

CZECH TECHNICAL UNIVERSITY IN
PRAGUE

Faculty of Nuclear Sciences and Physical
Engineering

Department of Physics



Research thesis

D^{\pm} measurement in Heavy Ion Collisions

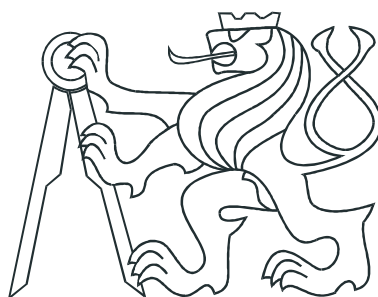
Bc. Zuzana Moravcová

Supervisor: Mgr. Jaroslav Bielčík, Ph.D.

Consultant: Ing. Lukáš Kramárik

Prague, 2018

ČESKÉ VYSOKÉ UČENÍ TECHNICKÉ
V PRAZE
Fakulta Jaderná a Fyzikálně Inženýrská
Katedra Fyziky



Výzkumný úkol

Měření mezonu D^\pm v jaderných zrážkách

Bc. Zuzana Moravcová

Vedoucí úkolu: Mgr. Jaroslav Bielčík, Ph.D.

Konzultant: Ing. Lukáš Kramárik

Praha, 2018



Katedra: fyziky

Akademický rok: 2017/2018

VÝZKUMNÝ ÚKOL

Student: Bc. Zuzana Moravcová

Studijní program: Aplikace přírodních věd

Obor: Experimentální jaderná a částicová fyzika

Vedoucí úkolu: Mgr. Jaroslav Bielčík, Ph.D

Ing. Lukáš Kramárik - konzultant

Název úkolu (česky/anglicky): Měření mezonu D^+ v jaderných srážkách

D^+ measurement in heavy ion collisions

Pokyny pro vypracování:

- 1) Interakce těžkých kvarků s jadernou hmotou
- 2) Přehled měření půvabných mesonů v jádro-jaderných srážkách
- 3) Rekonstrukce půvabného mezonu v srážkách Au+Au pomocí TMVA
- 4) Odhad systematických chyb měření
- 5) Diskuze a závěr

Výzkumný úkol bude vypracován v anglickém jazyku.

Součástí zadání výzkumného úkolu je jeho uložení na webové stránky katedry fyziky.

Literatura:

- [1] C. Pruneau, Data Analysis Techniques for Nuclear and Particle Physicists, CRC Press 2017.
- [2] G. Aarts, et al.: Heavy-flavor production and medium properties in high-energy nuclear collisions - What next?, Eur.Phys.J. A53 (2017) no.5, 93.
- [3] R. Russo, Measurement of D^+ meson production in p-Pb collisions with the ALICE detector, Ph.D. thesis, University of Torino, 2014.
- [4] A. Andronic, et al.: Heavy-flavour and quarkonium production in the LHC era: from proton-proton to heavy-ion collisions, Eur.Phys.J. C76 (2016) no.3, 107.

Datum zadání: 27.10.2017

.....

Datum odevzdání: 30.06.2018

vedoucí katedry

Prehlásenie:

Prehlasujem, že som svoju bakalársku prácu vypracovala samostatne a použila som len literatúru uvedenú v priloženom zozname.

Nemám závažný dôvod proti použitiu tohto školského diela v zmysle §60 Zákona č.121/2000 Sb., o práve autorskom, o právach súvisiacich s právom autorským a o zmene niektorých zákonov (autorský zákon).

V Prahe dňa

Název práce:

Meření mezónu D^+ v jaderných zrážkách

Autor: Zuzana Moravcová

Obor: Experimentální jaderná a částicová fyzika

Druh práce: Výzkumný úkol

Vedoucí práce: Mgr. Jaroslav Bielčík, Ph.D. Katedra fyziky, Fakulta jaderná a fyzikálně inženýrská, České vysoké učení technické v Praze

Abstrakt: Štúdium ťažkých kvarkov je jedna z možností, ako testovať kvark-gluónovú plazmu, hustú a horúca hmotu, ktorú je možné vytvoriť pri jadrových zrážkach na Relativistickom urýchľovači ťažkých jadier v Brookhaven-skom národnom laboratóriu alebo na Veľkom hadrónovom urýchľovači v Európskom centre pre jadrový výskum.

Porovnávanie produkcie pôvabných mezónov v protón-protónových zrážkach a v jadro-jadrových zrážkach pomocou jadrového modifikačného faktoru je jedným z možných testov kvark-gluónovej plazmy. Pre nízke hodnoty priečnej hybnosti skúmanej častice však pozorujeme vysoké kombinatorické pozadie, takže výťažok nie je možné určiť.

Táto práca sa zaoberá použitím strojového učenia na získanie surového výťažku produkcie D^\pm mezónu v zrážkach Au-Au pri energii $\sqrt{s_{NN}} = 200$ GeV z experimentu STAR z roku 2014. Použitím vylepšených rozhodovacích strojov z balíka TMVA implementovaného v programe ROOT sa výrazne zvýšila signifikancia v skúmaných oblastiach priečnych hybností a centralít.

Kľúčová slova: kvark-gluónová plazma, ťažké kvarky, pôvabné mezóny, STAR, RHIC, TMVA, BDT.

Title:

D⁺ measurement in heavy ion collisions

Author: Zuzana Moravcová

Specialization: Experimental nuclear and particle physics

Sort of project: Research thesis

Supervisor: Mgr. Jaroslav Bielčík, Ph.D. Department of Physics, Faculty of Nuclear Sciences and Physical Engineering, Czech Technical University in Prague

Abstract: One of the possibilities of investigating quark-gluon plasma, a hot and dense nuclear matter, is to study heavy quark production. Quark-gluon plasma can be produced in heavy-ion collisions on both Relativistic Heavy Ion Collider at Brookhaven National Laboratory and Large Hadron Collider at European Organization for Nuclear Research.

Comparison of the production of charm mesons in proton-proton collisions with production in heavy-ion collisions using nuclear modification factor is one of probes of quark-gluon plasma. A large combinatorial background is observed in reconstruction of charm mesons which complicates the analysis.

This goal of this thesis is introduction and application of machine learning methods in order to obtain raw yield of D[±] meson in $\sqrt{s_{NN}} = 200$ GeV Au-Au collisions from Run 14 of the STAR experiment. Boosted decision trees, implemented in the TMVA package inside the ROOT framework, considerable improved the significance within all regions of transverse momentum of D[±] meson and event centrality that were investigated.

Key words: quark-gluon plasma, heavy quarks, charm mesons, STAR, RHIC, TMVA, BDT.

Acknowledgment

I would like to express my gratitude to my supervisor Mgr. Jaroslav Bielčik, Ph.D. and to my consultant Ing. Lukáš Kramárik for their guidance, advices, and patience, and to Bc. Robert Líčeník for co-working on the analysis.

I would like to thank my family and friends as well for their endless support.

Contents

Introduction	11
1 Heavy Quarks Interactions	12
1.1 Standard Model	12
1.2 Quark-gluon plasma	14
1.2.1 Production of QGP	14
1.2.2 Variables needed to study QGP	16
1.2.3 Probes of QGP	18
2 STAR experiment	23
2.1 Brookhaven National Laboratory	23
2.2 Relativistic Heavy Ion Collider	24
2.3 STAR experiment	30
2.3.1 Heavy Flavor Tracker	31
2.3.2 Time Projection Chamber	32
2.3.3 Time of Flight detector	32
3 Charm mesons measurement	34
3.1 D mesons production in p-p collisions at ALICE at the LHC . . .	34
3.2 D mesons production in Pb-Pb collisions at ALICE at the LHC .	37
3.3 D mesons production in Au-Au collisions at STAR at the RHIC .	39
4 Reconstruction of D^+ meson	44
4.1 Machine learning in particle physics	44
4.2 Training phase	46
4.2.1 Discriminating variables	46
4.2.2 Signal and background sample production	48
4.2.3 BDT setup	49
4.2.4 Training output	49
4.3 Application phase and results	52
4.4 Systematic uncertainties	54
Summary	56
Bibliography	57

List of Figures

1.1	Phase diagram of nuclear matter	15
1.2	Time-space evolution of ultrarelativistic heavy ion collision	16
1.3	Pseudorapidity dependance on the azimuthal angle	17
1.4	Scheme of a heavy ion collision	18
1.5	Distribution of $d\sigma/dN_{ch}$ of a collision as a function of multiplicity	18
1.6	Nuclear modification factor of D^0 for different centrality classes	19
1.7	R_{AA} of D mesons in Pb-Pb collisions at $\sqrt{s_{NN}} = 2,76$ TeV for two centrality classes	20
1.8	Radial flow for protons, kaons and pions	21
1.9	Differential elliptic flow	22
2.1	RHIC complex	25
2.2	Schematic of RHIC preaccelerators	28
2.3	RHIC preaccelerators and intersection points	29
2.4	STAR detector	30
2.5	HFT resolution	31
2.6	TOF resolution	33
3.1	Hadronic decay of D^0	35
3.2	p_T -differential production cross section of prompt D^0 measured by ALICE in pp collisions at $\sqrt{s} = 13$ TeV compared to FONLL prediction.	36
3.3	Invariant mass distributions for D^0 and D^+ candidates	38
3.4	Transverse momentum distributions dN/dp_T of prompt D^0 and D^+	38
3.5	Nuclear modification factor R_{AA} of prompt D mesons	39
3.6	Transverse momentum distributions dN/dp_T of D^0 for different centrality classes	40
3.7	Nuclear modification factor R_{AA} of D^0	41
3.8	Raw yield of D^\pm meson from the hadronic channel	42
3.9	Nuclear modification factor R_{AA} of D^\pm	43
4.1	Schematic representation of a decision tree	45
4.2	Scheme of a particle triplet.	47
4.3	Distribution of transverse momentum p_T (left) and DCA (right) of kaons from the simulation of D^\pm decay.	48

4.4	Distributions of input variables within the TMVA for the D^\pm candidate p_T range 2 – 2.5 GeV/ c	49
4.5	Linear correlation matrices for signal (left) and background (right) from the training of TMVA for D^\pm analysis in the p_T range 2–2.5 GeV/ c from 0-10% most central collisions.	50
4.6	Overtraining check from the TMVA training phase for the D^\pm analysis in the p_T range 2 – 2.5 GeV/ c	50
4.7	Cut efficiencies and optimal cut value plots from the training of TMVA for D^\pm analysis in the p_T range 2–2.5 GeV/ c for different ratios of signal and background.	51
4.8	Significance as a function of the BDT cut for the D^\pm analysis in the p_T range 2 – 2.5 GeV/ c for the 0-80% centrality.	52
4.9	Invariant mass of $K\pi\pi$ triplet for centrality 0-10% and p_T range of D^\pm candidate 2.5-3 GeV/ c for the classical (left) and TMVA analysis (right).	53
4.10	Invariant mass of $K\pi\pi$ triplet for centrality 0-10% and p_T range of D^\pm candidate 2-2.5 GeV/ c for the classical (left) and TMVA analysis (right).	54
4.11	Obtained significance for different p_T bins of D^\pm meson in 0-10% event centrality for classical approach analysis (rectangular cuts) and for analysis with the use of boosted decision trees.	55

Introduction

One of the most interesting topics in the particle physics nowadays is without any doubt the study of quark-gluon plasma, a hot and dense nuclear matter that existed shortly after the Big Bang and can be produced in ultra-relativistic heavy-ion collisions. The details about the phase transition between this state of matter and hadronic matter are still unknown, therefore many scientists from both the Brookhaven National Laboratory and CERN dedicate their research to this topic.

The first chapter of this thesis introduces the Standard Model of particle physics and the quark-gluon plasma. It also describes the variables used for its investigation. Finally, since this state of matter cannot be observed directly because its very short lifetime, the probes of its existence are presented.

In the second chapter, the STAR experiment is presented. STAR is currently the only running experiment at the Relativistic Heavy Ion Collider (RHIC), the accelerator situated in the Brookhaven National Laboratory (BNL). The principle of acceleration of heavy ions is explained and demonstrated on different preaccelerators of RHIC. Three of STAR's subdetectors which will be used in the analysis later presented in this work are described - the Heavy Flavor Tracker, Time Projection Chamber and Time-Of-Flight detector.

The third chapter is dedicated to the summary of recent results in charmed meson production in both heavy-ion oriented experiments, STAR in BNL and ALICE in CERN, with the focus on D mesons. Since we need the reference from the proton-proton collisions, the results of measurements in this system are shown as well.

The last chapter of this work is devoted to the reconstruction of D^\pm mesons from $\sqrt{s_{NN}} = 200$ GeV Au-Au collisions at the STAR experiment using multivariate data analysis. The basic concept of machine learning is presented and specifically, the method of using Boosted Decision Trees (BDT) for classification, and its use in this project, is outlined. The choice of discriminating variables to be used in the BDT training phase is explained. The signal and background sample productions are described as well as the setup of the algorithm used. Finally, the obtained D^\pm raw yield and the discussion on systematic uncertainties are presented.

Chapter 1

Interaction of Heavy Quarks with Nuclear Matter

The following chapter works as an introduction to the Standard Model of particle physics, so a summary of the elementary particles and fundamental forces is presented as well as the quark-gluon plasma. This state of hot and dense matter can be produced artificially in heavy-ion collisions at high energy particle accelerators. At the end of the chapter, probes of the QGP medium are shown.

1.1 Standard Model

The matter around us is made up of molecules which are themselves made up of atoms. Every atom contains both a nucleus and an electron shell surrounding it. The nucleus is made up of nucleons: protons and neutrons. Nucleons, unlike the electron which is an elementary particle, are actually still composite bodies. They are stable states of two further types of elementary particles: quarks and gluons. A proton is made from two u quarks and one d quark. The aforementioned particles (the electron, u quark and d quark) along with the electron neutrino are the elementary particles of the first generation of the Standard Model. Their charges and masses are in Table 1.1. In general, there exists six types (flavors) of quarks, all of them with their properties are also in Tab.1.1.

At normal temperatures and densities, quarks cannot exist by themselves, they have to be confined within a hadron. A hadron, which is the collective term for a bound state of quarks, has two subcategories: a baryon (made from three quarks) or a meson (made from a quark and an antiquark). Every quark also has a color charge (red, green or blue), consequent hadron is always color neutral ("white"). When a meson is made from a quark and an antiquark of

generation	I	II	III
quark	u	c	t
	up	charm	top
mass [MeV/ c^2]	$2.2^{+0.4}_{-0.5}$	$1\,275^{+25}_{-35}$	$173\,000^{+400}_{-400}$
electric charge [e]	$2/3$	$2/3$	$2/3$
quark	d	s	b
	down	strange	bottom
mass [MeV/ c^2]	$4.7^{+0.5}_{-0.3}$	95^{+9}_{-3}	$4\,180^{+40}_{-30}$
electric charge [e]	$-1/3$	$-1/3$	$-1/3$
lepton	e	μ	τ
	electron	muon	tau
mass [MeV/ c^2]	0.5109989461(31)	105.6583745(24)	1\,776.86(12)
electric charge [e]	-1	-1	-1
lepton	ν_e	ν_μ	ν_τ
	electron neutrino	muon neutrino	tau neutrino
mass [eV/ c^2]	< 2	$< 0.19 \cdot 10^6$	$< 18.2 \cdot 10^6$
electric charge [e]	0	0	0

Table 1.1: Elementary particles – fermions. Spin of all listed fermions is $1/2$. Electric charge is a fraction of elementary charge e , $e = 1,602 \cdot 10^{-19}\text{C}$ [1].

the same flavor, we call the flavor hidden (e.g. J/ψ particle that is made from $c\bar{c}$ pair is hidden charm meson). On the other hand, when a particle has an anti-symmetric number of quarks and anti-quarks, we call it open flavor hadron (D^+ made from $c\bar{d}$ or Λ_c made from udc are open charm).

Collectively, particles with at least one heavy quark (c , b , t) are called heavy flavor particles. These cannot be observed directly as they decay very quickly. Therefore, we can only observe their decay products made from light quarks (u , d , s).

Particles are interacting with each other thanks to the fundamental forces, three of which are included in the Standard Model (SM). In the SM, the forces are carried by bosons. There are four types of force carriers (gauge bosons) with spin 1. The carrier of electromagnetic interaction, quantum electrodynamics (QED), is the photon which is massless¹ and has zero electromagnetic charge. The gauge bosons of the strong interaction, quantum chromodynamics (QCD), are gluons. These are also massless and electric-charge neutral, but gluons do carry the color-charge. They carry both a color and a different anti-color.² Quarks inside a hadron exchange gluons which are the cause for their confinement. Gluons carry almost the half of the proton momentum [2]. The strong interaction is approx. 10^2 times stronger than the electromagnetic one

¹More precisely, the mass of photon is experimentally determined to be $< 1 \cdot 10^{-18}$ eV/ c^2 [1].

²There are eight independent color states, equivalent to Gell-Mann matrices.

but is limited to very small distances. The exchange of gluons between tightly packed protons is the reason that they are stable in the nucleus of an atom and are not repelled due to electromagnetic forces.

The carriers of weak interactions are W^\pm and Z^0 bosons. While Z is electrically neutral, W has charge 1 or -1 . Their masses are $m_W = 80.4 \text{ GeV}/c^2$ and $m_Z = 91.2 \text{ GeV}/c^2$. Since both are very heavy, they cannot be observed directly, and only their decay products are observed.

The last part of the Standard Model is Higgs boson, with mass $m_H = 125.09 \pm 0.21 \pm 0.11 \text{ GeV}/c^2$ [1], discovered in 2012 at experiments ATLAS and CMS in CERN. The Higgs boson is an excitation of the Higgs field. This field provides the mechanism by which the masses of particles are attained in the SM. It also describes the mass difference between massless photon and the heavy W and Z bosons considering the unification of the electromagnetic and weak interaction into the electroweak interaction.

1.2 Quark-gluon plasma

When we put the matter in the extreme conditions such as very high temperature or density, hadrons dissolve into the new state, so called quark-gluon plasma (QGP) as shown on phase diagram of nuclear matter in Figure 1.1. Stable nucleus is situated in low temperature region ($T = 0$) with baryon chemical potential $\mu_B = 0.93 \text{ GeV}$ [3]. For region with higher μ_B , the transition between hadronic gas and QGP is of first order, thus have a discontinuity in the energy density. The high density phase (low temperature, very high baryon chemical potential) is expected to be in the interior of neutron stars [2]. In the low baryon chemical potential, when rising the temperature, the transition between hadronic gas and quark-gluon plasma is crossover. The point in the phase diagram where crossover transition becomes the first order transition is called critical point, its coordinates are $\mu_B \sim 440 \text{ MeV}$, $T_c \sim 170 \text{ MeV}$.

1.2.1 Production of QGP

This new type of matter in which quarks and gluons are deconfined and which behaves as a strongly interacting liquid, can be artificially created during heavy-ion collisions. The study of its properties, including the geometry of the phase transition lines and the exact position of the critical point, are the main focus of research conducted in the STAR experiment at the Relativistic Heavy Ion Collider (RHIC) and in the ALICE experiment at Large Hadron Collider (LHC). The former use collisions of ions of gold (^{179}Au) or uranium (^{238}U), the latter ions of lead (^{208}Pb). RHIC accelerator, which is described more precisely in chapter 2.2, has a special programme (Beam Energy Scan) to study phase transition of nuclear matter, chosen energies of collisions are illustrated also in Fig. 1.1. Corresponding baryon chemical potentials are shown in Tab. 1.2.

The time-space evolution of an ultrarelativistic heavy ion collision is shown in Figure 1.2 where z is the axis along the beam (so in the direction of initial

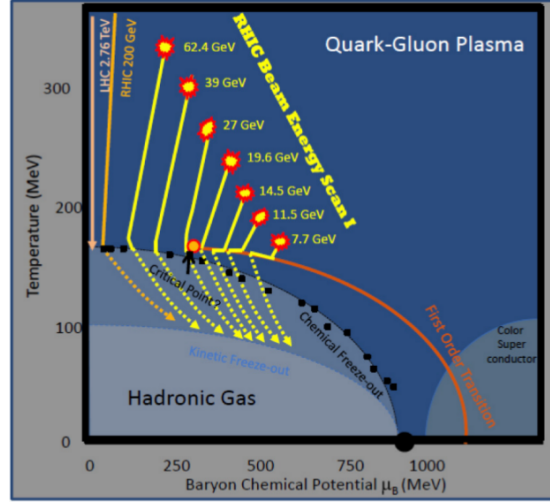


Figure 1.1: Phase diagram of nuclear matter. Taken from [4].

$\sqrt{s_{NN}}$ [GeV]	μ_B [MeV]
19,6	585
15	625
11,5	670
7,7	720
5	775

Table 1.2: Energy per nucleon pair $\sqrt{s_{NN}}$ and corresponding baryon chemical potential μ_B created during the Beam Energy Scan programme at RHIC. Taken from [4].

movement of ions). Thanks to the relativistic effects, nuclei are contracted in the longitudinal direction, so they are colliding (in point $(z, t) = (0, 0)$) in the shape of thin disks.

Right after the collision the pre-equilibrium phase occurs and in the time $t \sim 1 \text{ fm}/c = 3 \times 10^{-24} \text{ s}$ after the collision quark-gluon plasma is created and local thermodynamic equilibrium is settled. Since QGP has properties of perfect liquid, the system in this stage and its evolution can be described with relativistic hydrodynamic, more precisely the equation of state of the flowing matter [2]. Medium is still expanding and cooling down to the temperature below T_c , the system is in state where hydrodynamic description cannot be used anymore and process of hadronization is occurring (quarks and gluons are confined into hadrons).

After those processes, approximately after $10 \text{ fm}/c$ after the collision, the chemical freeze-out occurs, inelastic collisions stop and particle yields are not changing anymore. Subsequent kinetic (also called thermal) freeze-out is taking

place when elastic collisions ceased as well. Created particles continue to the detector where are detected at time $t \sim 4 \text{ cm}/c$ [5]. If particle is too heavy to pass all the way to the detector, only its decay products are detected.

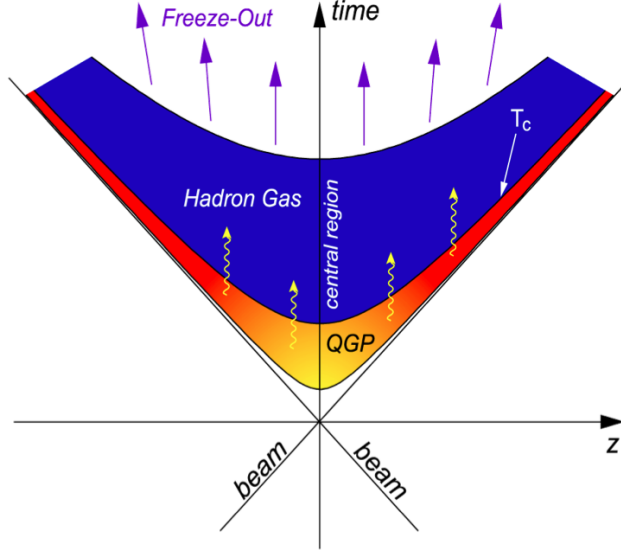


Figure 1.2: Time-space evolution of ultrarelativistic heavy ion collision. Taken from [6].

1.2.2 Variables needed to study QGP

As is obvious from previous section, QGP cannot be observed directly. However, there are several phenomena connected with the production of QGP, such as jet quenching, collective flow or particle yields. To describe those phenomena, a few variables need to be specified.

First of all, particles are moving along z axis with almost speed of light, therefore instead of momentum \vec{p} we use transverse momentum $p_T = \sqrt{p_x^2 + p_y^2}$, the component of momentum in the plane perpendicular to the initial movement of heavy ions, which is Lorentz invariant.

The center of mass energy, denoted \sqrt{s} , is the total energy available in collision experiment (in the center of mass frame). In heavy ions experiment, we use $\sqrt{s_{NN}}$ which is the center of mass energy per colliding nucleon pair.

Pseudorapidity describes the angle of the movement of the particle to the beam axis as

$$\eta = -\ln \left[\tan \left(\frac{\theta}{2} \right) \right], \quad (1.1)$$

where θ is the angle between \vec{p} and the positive direction of the z axis. The dependence of η at θ is shown in Figure 1.3.

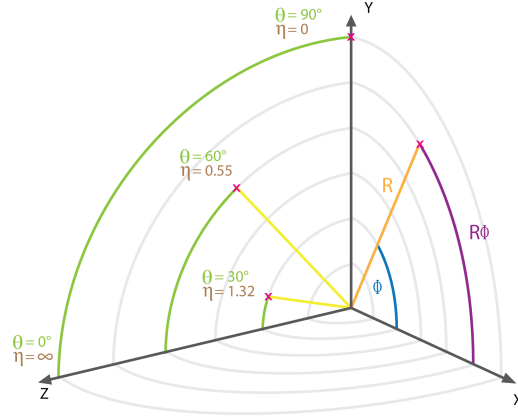


Figure 1.3: Pseudorapidity η dependance on the angle θ between the momentum and the positive direction of the beam axis. Taken from [7].

Since heavy ions are much bigger than protons, we need to think about the size of the region of the nuclei overlap in the time of collision. Based on this, we can classify collisions into several centrality classes. So called central collisions, or more precisely 0-5 % most central collisions, are when nuclei are colliding head to head. We can define a impact parameter b as a distance between the centers of colliding nuclei perpendicular to the beam axis. Then for central collisions $b \sim 0$.

When $b \sim 2R$, but still $b < 2R$, where R is the radius of colliding nucleus, we speak about peripheral collisions (70-80 % most central collisions), when $b > 2R$, we speak about ultra-peripheral collisions.

Scheme of a collision is shown in Fig. 1.4. On the left, the state before the collision is shown, where heavy ions are Lorentz contracted³, and b is shown. On the right, collision already took place. Concerning the nomenclature, nucleons that participated in the collision are called participants, others are called spectators.

Probability of a collision as a function of multiplicity, number of produced charged particles, is shown in Figure 1.5, as well as classes of centrality and number of participants. As is clear from the figure, more the collision is central, more particles are produced.

³In RHIC, Au nuclei are accelerated to the energy per nucleon 100 GeV. Unified atomic mass unit is $u = 931.494\,061(21) \text{ MeV}/c^2$ [1]. Then gamma factor, deduced from the formula $E = m\gamma c^2$ is ~ 107.35 . We can derive from the definition of $\gamma = 1/\sqrt{1-v^2/c^2}$ that Au nuclei are moving with velocity $\sim 0.9999566 c$. The atomic number of gold is $A = 197$, therefore we can deduce the radius of Au as $R = r_0 \sqrt[3]{A} = 6.98 \text{ fm}$, where $r_0 = 1.2 \text{ fm}$ is proportionality constant. In xy plane, the diameter of Au nucleus is 13.96 fm while along the z axis, the diameter is $2R/\gamma = 0.13 \text{ fm}$.

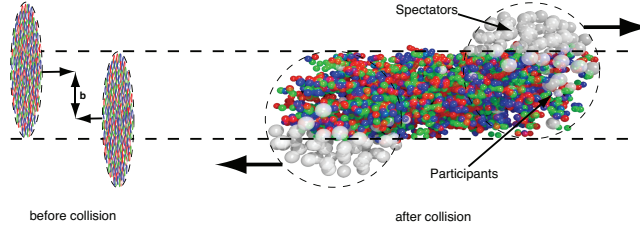


Figure 1.4: Scheme of a heavy ion collision. (Left:) Heavy ion just before collision, b is the impact parameter. (Right:) After collision, visualization of participants and spectators. Taken from [8].

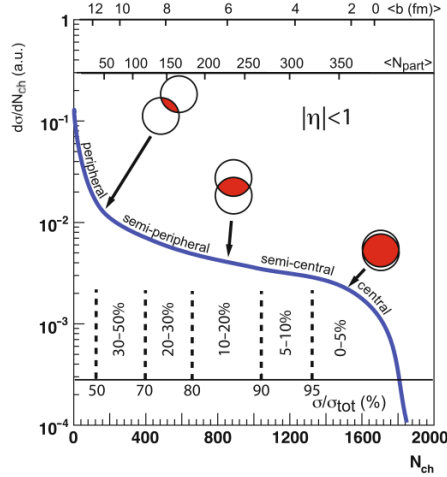


Figure 1.5: Distribution of $d\sigma/dN_{ch}$ of a collision as a function of multiplicity with illustrated classes of centrality. Taken from [9].

1.2.3 Probes of QGP

In proton-proton collisions, we can often observe two back-to-back particle jets. However, in heavy ion collisions, especially in central ones, we can observe so called dijet asymmetry – one jet disappears, or has significantly smaller energy. This phenomena, known as jet quenching, is explained by the fact that the parton produced in the initial hard scattering processes after the collision has to travel through QGP, so it has to interact with this hot and dense state of matter. Without loss of generality, one can say that one of two partons needs to pass larger distance within the QGP. The interaction with the medium then leads to the loss of energy of the parton. Energy loss can be either collisional (elastic scattering) or radiative (inelastic scattering, bremsstrahlung). Parton afterwards interacts with the vacuum and since it was very energetic, it produces a hadronic shower – a jet. While in p-p collisions the transverse momentum of

both jets is the same, the conservation is broken because of the medium effects.

Another possible probes of existence of QGP, similar to previous one, is to study particle yields. To compare those variables in proton (pp) or nuclei (AA) collisions, we define a variable nuclear modification factor as

$$R_{AA} = \frac{1}{\langle N_{bin} \rangle} \frac{\frac{dN}{dp_T}|_{AA}}{\frac{dN}{dp_T}|_{pp}}, \quad (1.2)$$

where $\frac{dN}{dp_T}|_{AA}$ and $\frac{dN}{dp_T}|_{pp}$ are particle yield in AA and pp collision, respectively. The ratio is scaled with mean value of binary collisions in heavy ion collision, $\langle N_{bin} \rangle$. Since particle yield varies significantly for different classes of centrality, one has to obtain R_{AA} independently for each class. Nuclear modification factor of D^0 meson for three centralities (0-10 %, 10-40 %, and 40-80 %) is shown in Figure 1.6. The data are from Au+Au collisions at STAR experiment at $\sqrt{s_{NN}} = 200$ GeV.

Nuclear modification factor for D mesons (D^0 , D^+ and D^{*+}) in Pb-Pb collisions at $\sqrt{s_{NN}} = 2,76$ TeV at the ALICE experiment for two different centrality classes are shown in Fig. 1.7. One can observe that the biggest suppression of particle production is observed in the most central collision around $p_T = 8$ GeV/c with the value of $R_{AA} \sim 0.14$, $R_{AA} \sim 0.4$ for higher p_T . For semi-peripheral collisions, we can observe slightly smaller suppression.

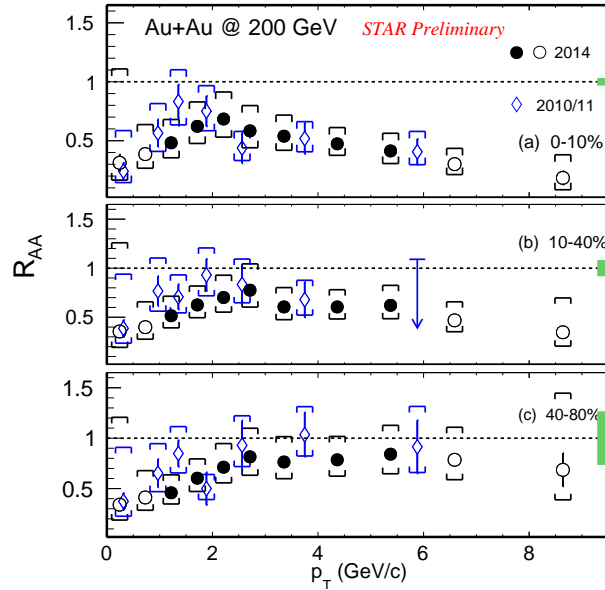


Figure 1.6: Nuclear modification factor of D^0 for different centrality classes. Taken from [10].

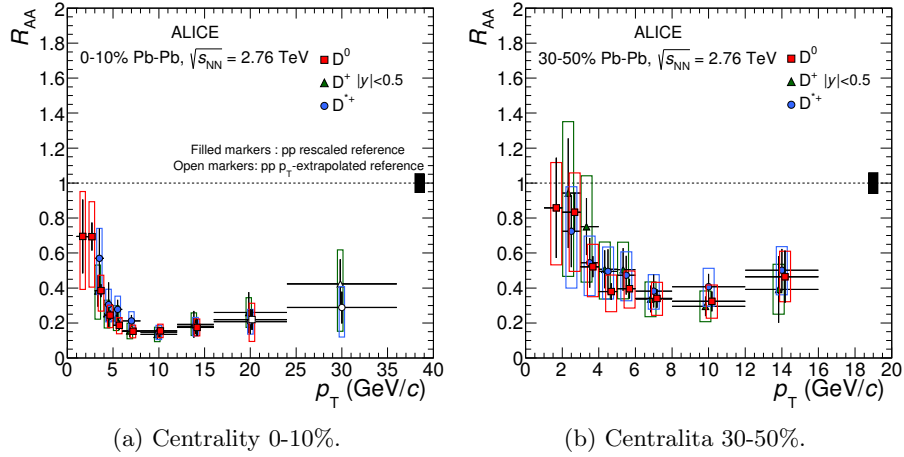


Figure 1.7: Nuclear modification factor R_{AA} of D mesons (D^0 , D^+ and D^{*+}) in Pb-Pb collisions at $\sqrt{s_{NN}} = 2.76$ TeV for two centrality classes. Taken from [11].

We can also observe suppression of quarkonia, so $c\bar{c}$ (J/ψ , ψ') or $b\bar{b}$ (Υ , Υ' , Υ'') mesons made in hard processes. Quarkonia is a special type of meson made from c or b quark and the antiquark of the same flavor, so the heaviest possible mesons. Those particles are bind very strongly which implies that their radii are smaller than other mesons. This causes that they can exist inside the QGP (so they are not melted at critical temperature). The "melting" temperature depends on the radius of the specific quarkonia. After gaining the critical value of temperature, high density of color charge in QGP causes color screening and subsequent dissociation of quark-antiquark pair. Knowing this phenomena, we can also deduce the temperature of the quark-gluon plasma.

Last but not least, QGP droplet is expanding very quickly after the heavy ion collision which causes a collective motion of particles, thus flow. In central collisions, we can observe radial flow, caused by isotropic expansion, which affects the shape of particle spectra at low p_T by slightly increasing p_T of particles. This effect is larger for protons than for kaons which is larger than for pions. Mass dependency is observed in Fig. 1.8.

In peripheral collision, overlapping region of colliding nuclei has an almond-like shape. When the system expands, the spatial anisotropy produce larger pressure gradient in reaction plane defined by beam direction and impact parameter b , xz plane, than in y direction. As a consequence, the azimuthally anisotropic flow is observed. We can characterize the flow patterns by coefficients in the Fourier expansion of the azimuthal dependence of the invariant yield,

$$E \frac{d^3N}{dp^3} = \frac{d^3N}{p_T dp_T dy d\phi} = \frac{d^2N}{p_T dp_T dy} \frac{1}{2\pi} \left[1 + \sum_{n=1}^{\infty} 2v_n \cos n(\phi - \Phi_R) \right], \quad (1.3)$$

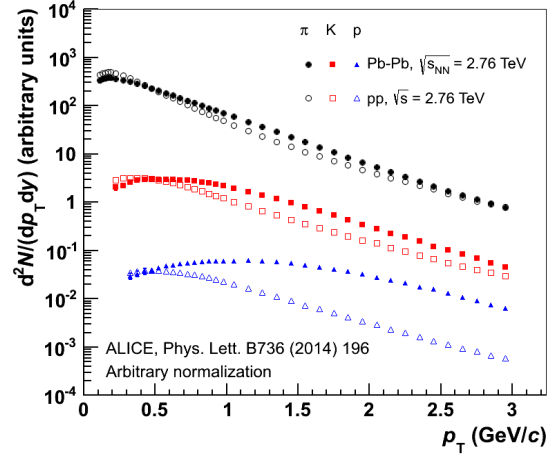


Figure 1.8: Radial flow for protons, kaons and pions – particle yield as a function of p_T . Taken from [5].

where ϕ is the azimuthal angle to the reaction plane and Ψ_R the reaction plane angle. Coefficients v_1 , v_2 and v_3 are called directed, elliptic and triangular flow, respectively. Directed flow affects mostly particles at forward and backward rapidities while elliptic flow is strongest near midrapidity. Elliptic flow from Pb+Pb collisions at ALICE at $\sqrt{s_{NN}} = 2,76$ TeV and from Au+Au collisions at STAR at $\sqrt{s_{NN}} = 200$ GeV for three different centrality classes is shown in Figure 1.9.

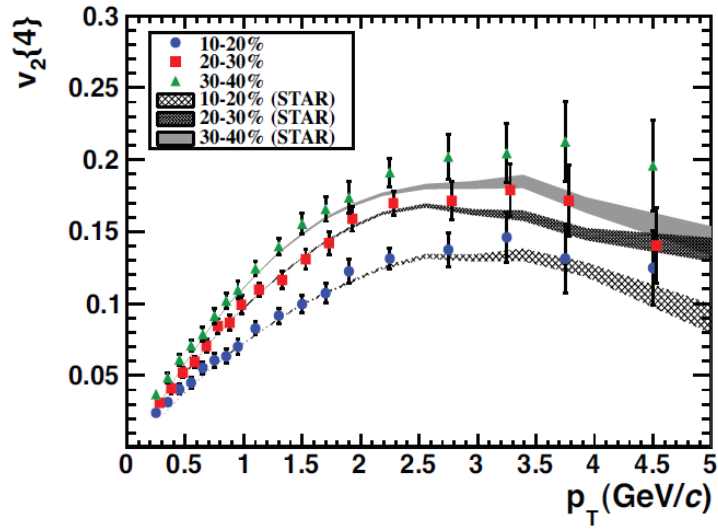


Figure 1.9: Differential elliptic flow for three different centrality classes. Colored symbols are data from Pb+Pb collisions at ALICE at $\sqrt{s_{NN}} = 2,76$ TeV, grey lines are from Au+Au collisions at STAR at $\sqrt{s_{NN}} = 200$ GeV. Taken from [3].

Chapter 2

STAR experiment

The STAR experiment is installed in the Relativistic Heavy Ion Collider which is situated in the Brookhaven National Laboratory. Following chapter will introduce all of mentioned notions.

2.1 Brookhaven National Laboratory

Situated in Upton, New York, Brookhaven National Laboratory (BNL) is one of the biggest scientific facilities in United States of America. After World War II, in 1947, the Lab was opened on the former U.S. military base (Camp Upton) with main purpose to study the atom and its energy for peaceful application [12]. Nowadays it is a multipurpose research organization that connects thousands of scientists around the world. Together they received seven Nobel Prizes and many other awards and recognitions (as National Medal of Science, Enrico Fermi Award, Ernest Orlando Lawrence Memorial Award, etc.). Since next section will be about Relativistic Heavy Ion Collider, hence only other facilities will be introduced in following text.

BNL's energy department studies generation, transmission, storage and end use of energy. Concerning generation, the focus is on renewable sources (solar, wind, nuclear power) without producing carbon dioxide that causes climate change. BNL has its own photovoltaic plant, 32-megawatt Long Island Solar Farm, which is the largest in the Eastern U.S. To store the energy, advanced battery materials and superconducting magnets are being developed.

To study structure of materials (with nanoscale resolution), their chemical composition and magnetic properties, National Synchrotron Light Source II (NSLS-II) is used, where electrons are accelerated almost at speed of light at a curved trajectory producing synchrotron radiation in all wavelengths. NSLS-II is a medium energy (3 GeV) electron storage ring with circumference 792 m that started to operated in 2015. It is 10^4 times brighter than its ancestor, NSLS, that operated between 1982 and 2014. The research on that synchrotron helped to win two Nobel Prizes in Chemistry to:

- Roderick MacKinnon in 2003 *for structural and mechanistic studies of ion channels*,
- Venkatraman Ramakrishnan and Thomas A. Steitz in 2009 *for studies of the structure and function of the ribosome* [13].

The Center for Functional Nanomaterials also studies properties of materials. In specialized laboratories, devices for nanoelectronics, nanophotonics, or biomedical engineering are being produced. Brookhaven Linac Isotope Producer, the high-energy medical particle accelerator, produces radioisotopes for diagnosis and disease treatment (targeted cancer therapy).

Moving to physics, Brookhaven is a member of Daya Bay Neutrino Experiment as well as ATLAS Collaboration. The Lab also leads the development of 3 200 megapixels Large Synoptic Survey Telescope (that will be constructed on a mountaintop in Chile). On site of BNL, one can also find NASA (National Aeronautic and Space Administration) Space Radiation Laboratory that studies the effects of space radiation on cells and tissues with aim to reduce the risk for astronauts during long-term missions. Working in BNL, several scientists won Nobel Prizes in Physics:

- Chen Ning Yang and Tsung-Dao Lee in 1957 *for their penetrating investigation of the so-called parity laws which has led to important discoveries regarding the elementary particles*,
- Samuel Chao Chung Ting in 1976 *for their pioneering work in the discovery of a heavy elementary particle of a new kind*,
- James Watson Cronin and Val Logsdon Fitch in 1980 *for the discovery of violations of fundamental symmetry principles in the decay of neutral K-mesons*,
- Leon M. Lederman, Melvin Schwartz, and Jack Steinberger in 1988 *for the neutrino beam method and the demonstration of the doublet structure of the leptons through the discovery of the muon neutrino*,
- Raymond Davis Jr. in 2002 *for pioneering contributions to astrophysics, in particular for the detection of cosmic neutrinos* [13].

2.2 Relativistic Heavy Ion Collider

The Relativistic Heavy Ion Collider, shown in Fig. 2.1, is an accelerator that can collide different heavy ions or polarized protons at ultrarelativistic energies. As in the case of all high energy accelerators, particles need to be accelerated in several steps.

First of all, one needs the source of particles that will be accelerated. Until 2012, the ion source and the first pre-injectors were two Tandems Van de Graaf built in 1970. This electrostatic accelerator facility could produce approx. 40 different ions from as light as hydrogen to as heavy as uranium. The necessity

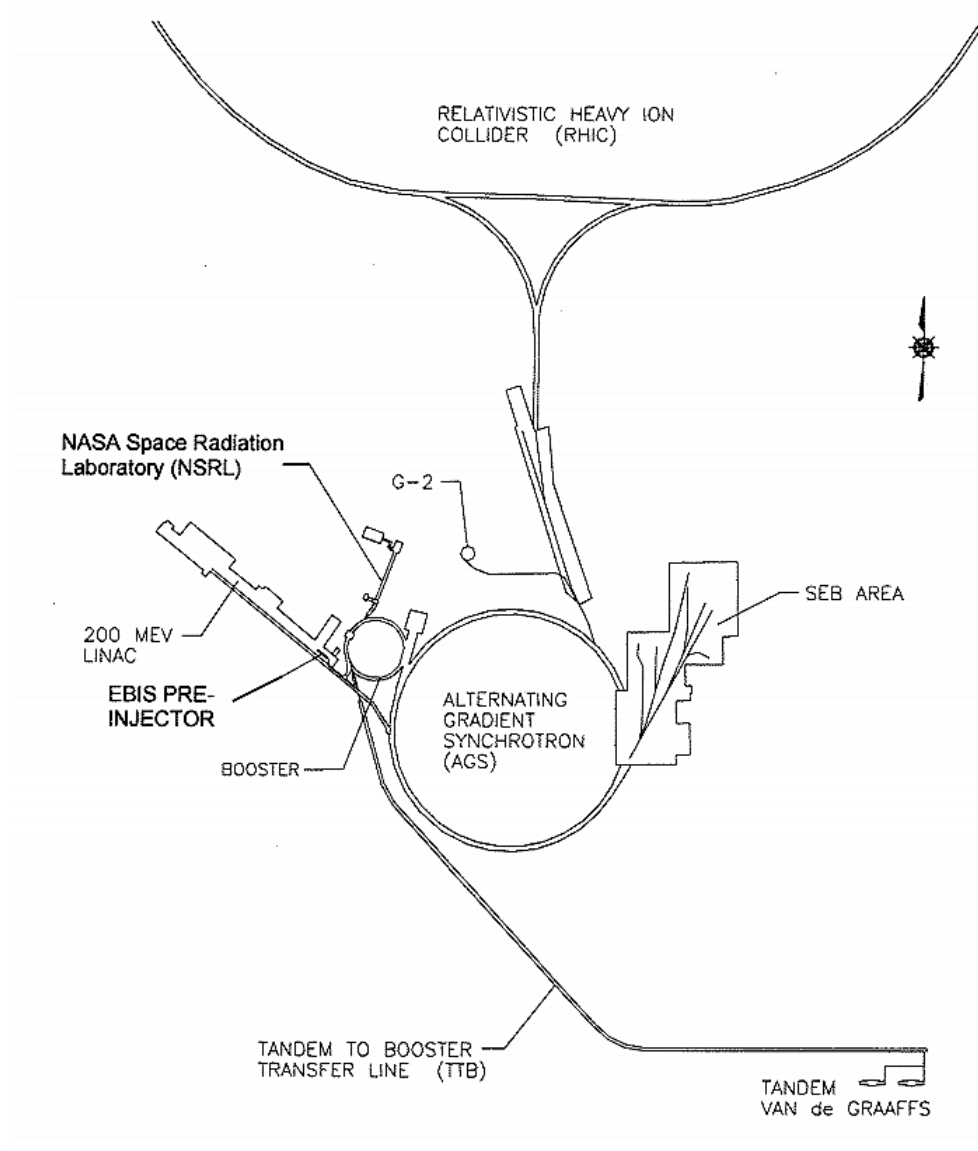


Figure 2.1: The Relativistic Heavy Ion Collider and its preaccelerators. Taken from [14].

to transport the beam 860 m from Tandems to Booster was just one of many reasons to replace the source. Nowadays, Tandems Van de Graafs are used for applied research, eg. in NASA Radiations Effects Facility.

After its development at BNL Collider-Accelerator Department, new pre-injector is being used, Electron Beam Ion Source (EBIS). To become adequate substitute of Tandems, EBIS is followed by Radio Frequency Quadrupole (RFQ) and a short Linac (linear accelerator). To compare EBIS with its precursor, EBIS is more reliable and flexible, the transport line is only 30 m long. Also, the injecting energy and intensity of ions are higher, so the injections is easier and there is smaller loss. Tandems can only produce negative ions, so before being injected to Booster, ions are stripped by a passage through a carbon foil. However, EBIS can directly produce ions with desired charge state [14]. Contrary of Tandems, EBIS can also produce ions of noble gases needed to NASA Space Radiation Laboratory science programs.

Concerning the ion source itself, laser ion source called LION is used since 2014¹, one of its positives is that it can switch between different species of ions very quickly. LION is composed from a high-power pulsed laser with a solid target. In case of Au ions production, the target is 1-mm thick pad with area of 25×25 mm [15].

After being produced in LION, positive ions with charge 1 go to EBIS where their charge is multiplied to 2, 32, and 39 for ³He, Au, and U, respectively [16] and their output energy per nucleon is 16.24 keV/u. Afterwards ions go to RFQ via the Low Energy Beam Transport (LEBT) where are accelerated to 314.72 keV/u. Ions continue through Medium Energy Beam Transport (MEBT) to Interdigital-H (IH) 4-metres-long Linac where they are further accelerated to 2 MeV/u which is a minimal energy to enter the next stadium, the Booster. EBIS complex produces short pulses (10-40 μ s) with high intensity ($3.2 \cdot 10^9$ ions per pulse for Au³²⁺), so only a few (1-4) turns are need to inject the Booster (in opposition with 30-40 turns needed with Tandems).

Later, the beam is injected horizontally to Booster, the circular accelerator with circumference 201.78 m [17], via the High Energy Beam Transport (HEBT). In Booster, built in 1991 to improve the operation of Alternating Gradient Synchrotron (AGS), gold ions are accelerated to energy per nucleon 70 MeV/u. After leaving the Booster (thanks to kicker magnet), ions's charge increase (to 77 for gold ions) as they pass the stripping foil and lose electrons. Subsequently they are transferred via the Booster-to-AGS into the AGS, circular accelerator with 4-times larger circumference as the Booster, 807.12 m.

After being kicked from AGS with energy approx. 10 MeV/u, ions enter 770-metres-long AGS-to-RHIC transfer line [18]. At its begging, the stripping foil is situated which takes away two last electrons from gold ions (producing final ions, Au⁷⁹⁺). When ions are closer to RHIC, a switch dipole is installed to direct beams into one of two RHIC rings, and finally, ions are injected to either clockwise (blue) or counterclockwise (yellow) ring (thanks to four vertical kicker magnets that inject bunch onto circulating orbit). In RHIC, 3834-metres-long

¹LION replaced Hollow Cathode Ion Source.

Run	species	total particle energy [Gev/nucleon]	total delivered luminosity $\cdot 10^{-9}$ [b ⁻¹]
Run-14	Au + Au	7.3 + 7.3	44 200
	Au + Au	100.0 + 100.0	43.9
	He + Au	103.5 + 100.0	134
Run-15	<i>p</i> + <i>p</i>	100.2 + 100.2	0.382
	<i>p</i> + Au	103.9 + 98.6	0.001
	<i>p</i> + Al	103.9 + 98.7	0.003
Run-16	Au + Au	100.0 + 100.0	52.2
	d + Au	100.7 + 100	289
	d + Au	31.3 + 31.1	44.0
	d + Au	9.9 + 9.8	7.2
Run-17	d + Au	19.6 + 19.4	19.5
	<i>p</i> + <i>p</i>	254.9 + 254.9	0.579
	Au + Au	27.2 + 27.2	477 000
	<i>p</i> + <i>p</i>	254.9 + 254.9	0.00136
Run-18	Zr + Zr	100.0 + 100.0	3.9
	Ru + Ru	100.0 + 100.0	4.0
	Au + Au	13.5 + 13.5	282 000
	Au + Au	3.85	
	Au + Au	14.8	

Table 2.1: Summary of RHIC Runs. Bold means fixed target, italic polarization. Taken from [19].

collider, heavy ions gain the final energy per nucleon, up to 100 GeV/u.

The summary of consecutive stages of ionization and acceleration are shown in Figure 2.2 together with a maximum energy, number of ions per pulse and efficiency for every stage during the gold ions acceleration.

RHIC complex can accelerate and collide different pairs of ions as Au⁷⁹⁺, U⁹²⁺, Zr⁴⁰⁺, Ru⁴⁴⁺, or Cu²⁹⁺. It is also possible to produce asymmetrical collisions by colliding eg. deuterium with the gold ions. Summary of RHIC runs since 2014 is in the Table 2.1, all runs can be found online at [19].

RHIC is the only collider in the world that operates also with polarized protons – protons with the same direction of spin. The purpose of that kind of collisions is to study the spin of proton. The Optically Pumped Polarized Ion Source (OPPIS) creates $9 \cdot 10^{11}$ polarized H⁻ in a short pulse (300 μs) [20].

Hydrogen ions are accelerated to 200 MeV by RFQ and Linac. Afterwards they are stripped, so polarized protons are entering the Booster. There they are accelerated to 1.5 GeV and transferred to AGS, where the acceleration continue until 25 GeV. Since during acceleration a depolarization occurs, on AGS is installed partial Siberian Snake². Beams are then injected to RHIC, where two

²Siberian Snake is a device that rotates spin 180° about a horizontal axis. Since the rotation from the Snake is larger than the one caused by depolarizing resonances, spin remains stable.

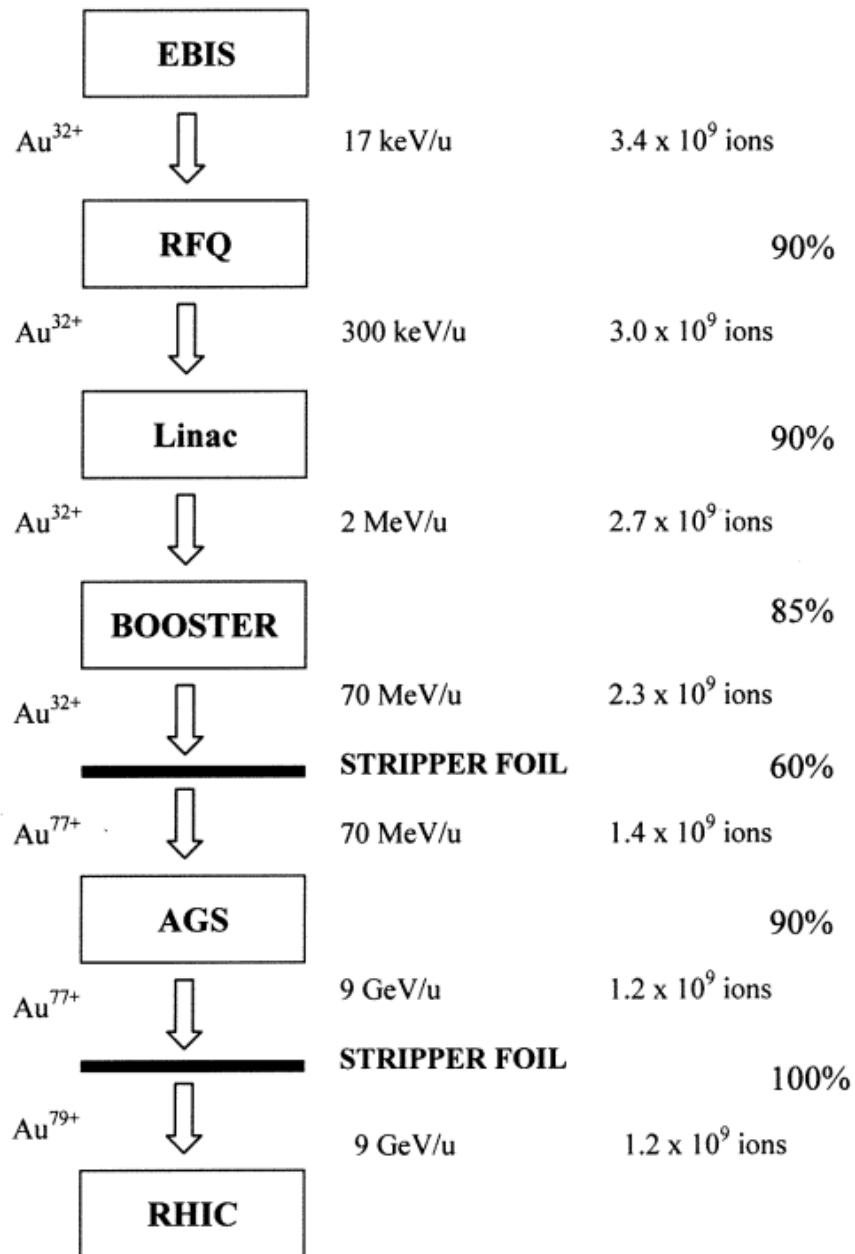


Figure 2.2: Schematic of RHIC preaccelerators. Taken from [14].

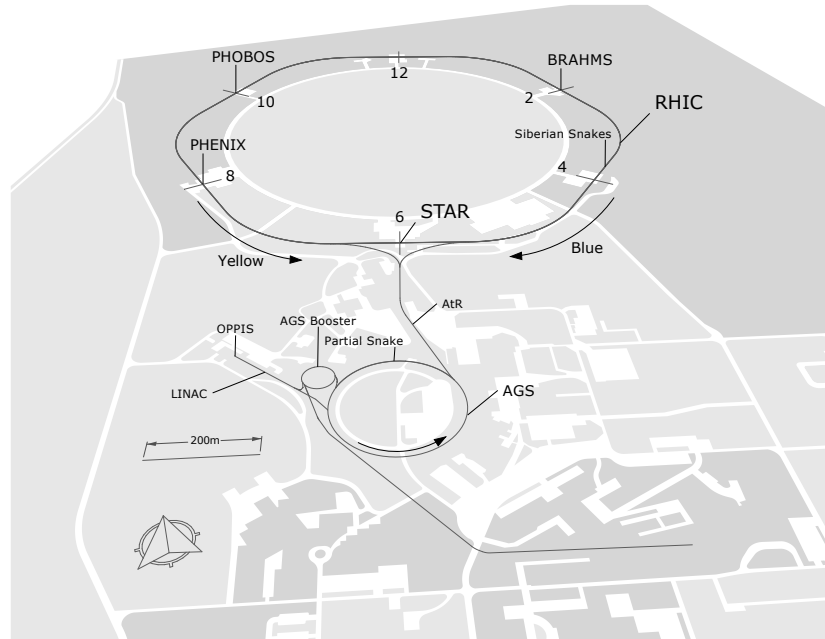


Figure 2.3: RHIC preaccelerators and intersection points. Taken from [21].

full Siberian Snakes are located on opposite sides of the collider, and are further accelerated up to 500 GeV.

As already mentioned, RHIC has two independent rings, clockwise (blue) and counterclockwise (yellow), with total six intersections between them. When one identify the circuit with a clock, intersections are placed on all even numbers and the injection is near 6 o'clock, as illustrated in Figure 2.3.

Experiments PHOBOS and BRAHMS have ended the data collection in 2005 and 2006, respectively. The focus of PHOBOS was the new physics, supposing that it is occurring very rarely, but when it does, one can identify it relatively easily. BRAHMS (*Broad Range Hadron Magnetic Spectrometer*) measured charged hadrons to study proprieties of highly excited nuclear matter produced in heavy ion collisions.

Experiment PHENIX (*Pioneering High Energy Nuclear Interaction eXperiment*) stopped data taking in 2016. Now a new experiment sPHENIX is constructed. The new detector will be completed in 2020 and will focus on study of jets and beauty quarkonia, including the current-day questions regarding the perfect fluidity of the quark-gluon plasma [22]. While physics goals of PHENIX and STAR experiments are similar, thus study of quark-gluon plasma, PHENIX is designed to measure direct probes of heavy ion collisions (electrons, muons, photons).

2.3 STAR experiment

The following chapter is dedicated to the STAR detector (Solenoidal Tracker at RHIC), shown in Figure 2.4, which is constructed to study formation and properties of quark-gluon plasma via measurement of hadron production over a large solid angle. One of the physics goals of STAR experiment is to investigate the phase transition of nuclear matter for different energies and baryon chemical potential as shown in Fig. 1.1 and Tab. 1.2. Phase II of Beam Energy Scan programme is scheduled until 2020.

STAR consists of several detectors with different characteristics and purposes, eg. high precision tracking, momentum analysis or particle identification. Only detectors used in the analysis which is described in this thesis will be introduced.

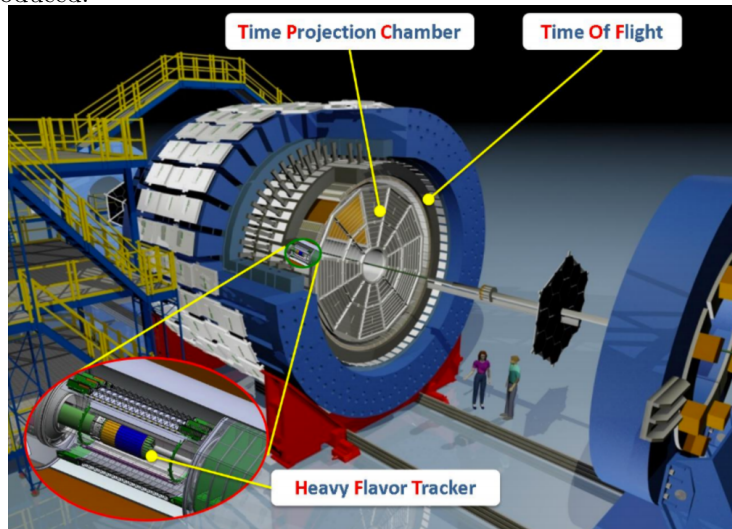


Figure 2.4: STAR detector with selected subdetectors. Taken from [23].

The name of detector has connection with its main component - solenoidal magnet producing uniform magnetic field (0.5 T). The solenoid has interior and outside diameter 5.24 m and 5.94 m respectively, and is 6.2 m long [24].

Data collected by STAR are subsequently analyzed by the STAR collaboration consisting of scientists from 14 different countries. They are divided into five physics working groups with focus on a specific topic:

- bulk correlations,
- heavy flavor,
- jet-like correlations,
- light flavor spectra and peripheral collisions,
- spin.

2.3.1 Heavy Flavor Tracker

Being installed as the closest to the beam pipe, Heavy Flavor Tracker (HFT) is the first detector that produce particles' hit which is strongly connected with the physics purpose of this detector - very precise measurement of heavy flavor production by distinguishing secondary vertex. This measurement is very important because heavy quarks are good probe for studying QGP. However, heavy particles decay very quickly to light ones, therefore the exact position of decay vertices of heavy flavor particles displaced from the primary vertex is very needed information [25]. The resolution of HFT is shown in Figure 2.5.

HFT was built and installed for RHIC Run 14 and removed two year afterwards. The design was made to have the best possible position resolution and consists of three layers: Silicon Strip Detector (SSD), Intermediate Silicon Tracker (IST) and PIXEL (PXL) detector.

PIXEL detector is located closest to the beam pipe and uses state-of-the-art ultra-thin CMOS Monolithic Active Pixel Sensors (MAPS). It has 10 sectors with 4 ladders each, from which one is 2.9 cm from the center of the detector and three on the outer layer, 8.2 cm from the center. The total hit resolution is $6.3 \mu\text{m}$. Since it is very close to the beam pipe, the detector was developed to be as resistant as possible to the radiation damage.

IST and SSD are made from single-sided double-metal silicon pad sensors and double-sided silicon strip sensors, respectively. Their position resolution is $170 \mu\text{m}$, $20 \mu\text{m}$ in the $r \times \phi$ direction and 1.8 mm , $740 \mu\text{m}$ in the z direction.

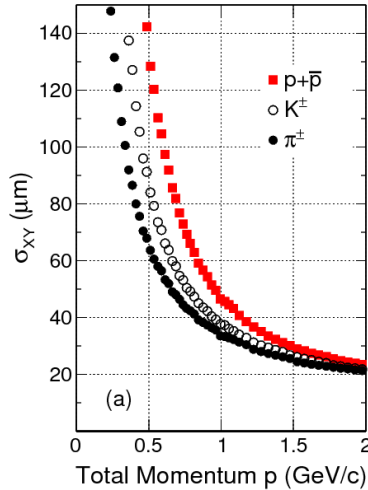


Figure 2.5: Resolution of Heavy Flavor Tracker detector. STAR, Au+Au collisions at $\sqrt{s_{NN}} = 200 \text{ GeV}$ and centrality 0-80%. Taken from [26].

2.3.2 Time Projection Chamber

Time Projection Chamber (TPC), often called a heart of STAR, is its main tracking detector – it records the tracks of charged particles and also measures their momenta and charge based on the curvature of the trajectory, since charged particles in a magnetic field is moving on a circular path. Momenta are measured over a range of 100 MeV/ c to 30 GeV/ c [27].

TPC can identify particles in the momentum range from 100 MeV/ c to 1 GeV/ c . Particle identification (PID) by TPC is done by measuring the ionization energy loss of the particle with the use of Bethe-Bloch formula which gives the specific energy loss of charged particle in homogeneous medium:

$$-\left\langle \frac{dE}{dx} \right\rangle = 2\pi N_A r_e^2 m_e c^2 \frac{Z}{A} \frac{z^2}{\beta^2} \left[\ln \frac{2m_e c^2 \beta^2 \gamma^2 W_{\max}}{I^2} - 2\beta^2 - \delta(\beta\gamma) \right], \quad (2.1)$$

where N_A is Avogadro's number ($N_A = 6,022 \cdot 10^{23} \text{ mol}^{-1}$), r_e is classical electron radius ($r_e = 2,81 \cdot 10^{-15} \text{ m}$), m_e is mass of electron ($m_e = 0,511 \text{ MeV}/c^2$), c is speed of light in vacuum ($c = 299792458 \text{ m}\cdot\text{s}^{-1}$), Z and A are atomic and mass number of the absorber, respectively, z and v are charge and speed of the particle, $\beta = \frac{v}{c}$ and $\gamma^{-1} = \sqrt{1 - \beta^2}$ are relativistic factors, I is mean ionization and excitation potential, W_{\max} is magnetic kinetic energy which can be imparted in one collision and δ is density correction which is needed for highly relativistic velocities. The dE/dx resolution depends on the gas and the pressure inside the chamber.

Concerning the acceptance of TPC, it covers full azimuthal angle (2π) and pseudorapidity $|\eta| < 1$, which is caused by its 4.2 m long and 4 m diameter barrel shape.

The volume of TPC is filled with P10 gas (90% argon, 10% methane). When the primary particle is passing through this gas, it is ionizing its molecules, creating electron-ion pair. Subsequently, secondary electrons are drifting towards readout located at the both ends of the chamber. The position resolution is limited with a diffusion of drifting electrons. The x , y position (so those in a transversal plane) are determined by the position of cluster where the charge was collected, the z coordinate is based on drifting time of secondary electrons from the point of origin to the anode. Since we measure the drifting velocity of electrons in the filling gas, we can determine the z position.

In the close future, TPC will be upgraded to iTPC. The new parts of detector will extend the track pseudorapidity acceptance to $|\eta| < 1.5$, so tracking at small angles relative to the beam pipe would be possible. This upgrade will also increase the resolution in both dE/dx and momentum and improve the acceptance of low momenta tracks [28]. iTPC is planned to start data taking for RHIC Run 19 in 2019.

2.3.3 Time of Flight detector

Since the average proton transverse momentum in heavy ion collision is approximately 0.9 GeV/ c , the TPC detector is not sufficient for the particle identifica-

tion with the upper limit of $1 \text{ GeV}/c$. To extend the range of possible identification of particles with higher p_T , the barrel Time of Flight (TOF) was installed in 2010 [29]. As suggested by its name, TOF identifies particle based on the time of light inside the detector. For relativistic particles, where $E \simeq pc \gg m_i c^2$, the separation power of TOF can be counted as

$$\Delta t = \frac{Lc}{2p^2}(m_1^2 - m_2^2), \quad (2.2)$$

where L is distance between TOF counters and the beam pipe (starting time is measured with other parts of the STAR detector), p momentum (known from TPC) and m_1, m_2 are the masses of two particles to be distinguished. The present capability of kaon separation is possible from $\sim 0.6 \text{ GeV}/c$ to $\sim 1.7 \text{ GeV}/c$, while the upper limit of proton is $\sim 3.0 \text{ GeV}/c$. The resolution is shown in Figure 2.6.

Since the trajectory of particle Δs is also known from TPC, with Δt known from TOF and relation $\beta = \frac{v}{c} = \frac{\Delta s}{\Delta t} \frac{1}{c}$, one can deduce the mass of the particle as

$$m = \frac{p}{c} \sqrt{\left(\frac{1}{\beta}\right)^2 - 1}. \quad (2.3)$$

TOF covers the same pseudorapidity acceptance as TPC, thus $|\eta| < 1$, and full azimuthal angle 2π . It used the multi-gap resistive plate (MGRP) chamber with resolution sub-one hundred picoseconds and total efficiency approximately 95%. To cover full outside surface of the detector, there are totally 3800 MRPC modules with 6 pairs of copper pads each, producing more than 23 000 channels to be read out.

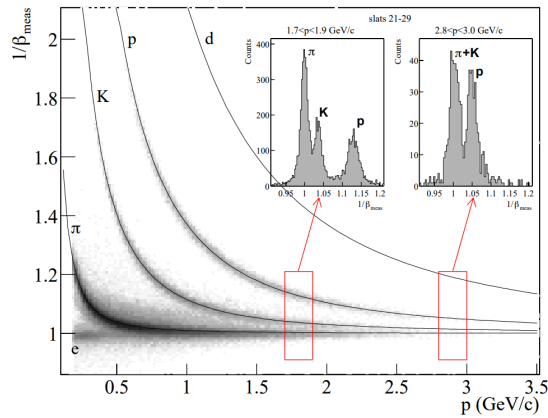


Figure 2.6: Resolution of Time of Flight detector. Taken from [30].

Chapter 3

Charm mesons measurement

Since heavy quarks are produced in the initial stages of the heavy-ion collisions, they could probe its whole evolution. Study of heavy quarks production is therefore interesting to investigate the properties of the quark-gluon plasma. Following chapter presents the study of the production of D^0 and D^+ mesons at experiment STAR (RHIC, BNL) and ALICE (LHC, CERN). Considering the need of reference from proton-proton collisions, a short overview of recent results will be presented as well.

Summary of properties of selected charm mesons is in Tab. 3.1. Listed D mesons are open charm mesons ($c = 1$), while J/ψ is hidden charm meson ($c = 0$).

meson	D^0	D^+	D_s^0	J/ψ
quark composition	$c\bar{u}$	$c\bar{d}$	$c\bar{s}$	$c\bar{c}$
mass [GeV/ c^2]	1.864	1.869	1.968	3.097

Table 3.1: Properties of selected charm mesons. Taken from [1].

3.1 D mesons production in p-p collisions at ALICE at the LHC

The most recent measurements of D^0 and D^+ mesons from p-p collisions at $\sqrt{s} = 2.76, 5, 7, 8$ and 13 TeV with the ALICE experiment that will be shown are taken from [31]. Those particles were reconstructed via their hadronic decay channels, $D^0 \rightarrow K^-\pi^+$ and $D^+ \rightarrow K^-\pi^+\pi^+$ with branching ratios $(3.93 \pm 0.04)\%$ and $(9.46 \pm 0.24)\%$, respectively [1].

Candidates were chosen as a right sign combinations of pairs/triplets of pions and kaons. Particle identification (PID) was made with both the specific energy

loss (TPC) and the time-of-flight (TOF) with 3σ compatibility cut between the measured and expected signal. If no TOF signal was provided, only the TPC information was used for the PID. If the two measurements were incompatible, the particle was considered to be compatible with both a kaon and a pion.

For D^0 reconstruction, decay products have to obey following criteria:

- $p_T > 0.7 \text{ GeV}/c$, where p_T is transverse momentum of decay products (K, π),
- $DCA_d < 300 \text{ }\mu\text{m}$, where DCA_d is the maximum distance of closest approach between the two tracks,
- $\lambda > 100 \text{ }\mu\text{m}$, where λ is the decay length, that is the distance between the primary and secondary vertex,
- $\cos \theta > 0.8$, where θ is the pointing angle, the angle between the vector sum of momentum of decay particles and the decay length vector.

Visualization of used variables for hadronic decay of D^0 is shown in Fig. 3.1.

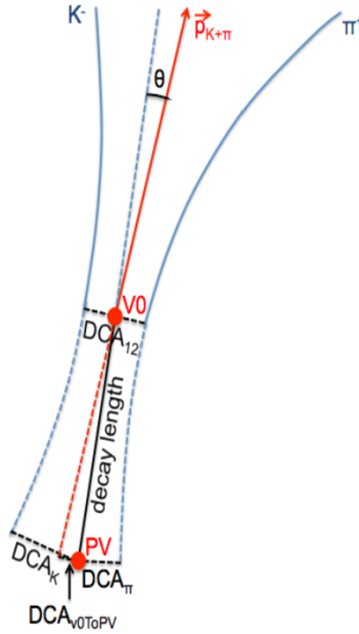


Figure 3.1: Hadronic decay of D^0 . Taken from [10].

For D^+ reconstruction, which is studied through a three-body decay, there is e.g. a lower average momentum, the selected cuts are:

- $p_T > 0.4 \text{ GeV}/c$,

- $\lambda > 800 \mu\text{m}$,
- $\cos \theta > 0.95$.

Mean life of D^0 and D^+ are $410 \cdot 10^{-15} \text{ s}$ and $1040 \cdot 10^{-15} \text{ s}$, respectively, which is equivalent to $c\tau$ $122.9 \mu\text{m}$ and $311.8 \mu\text{m}$ [1].

The p_T -differential production cross section of prompt D^0 measured at central rapidity by ALICE in minimum-bias p-p collisions at $\sqrt{s} = 13 \text{ TeV}$ is shown in Fig. 3.2 together with the FONLL (Fixed-Order-Next-to-Leading-Log) prediction calculations. For LHC measurements, the cross section in proton-proton collisions is essential to compute the nuclear modification factor R_{AA} as

$$R_{AA} = \frac{1}{\langle T_{AA} \rangle} \frac{\frac{dN}{dp_T}|_{AA}}{\frac{d\sigma}{dp_T}|_{pp}}, \quad (3.1)$$

where $\langle T_{AA} \rangle$ is an average nuclear overlap function which is proportional to the number of binary nucleon-nucleon collision. The formula is in full accordance with the formula used to compute R_{AA} at RHIC (Eq. 1.2).

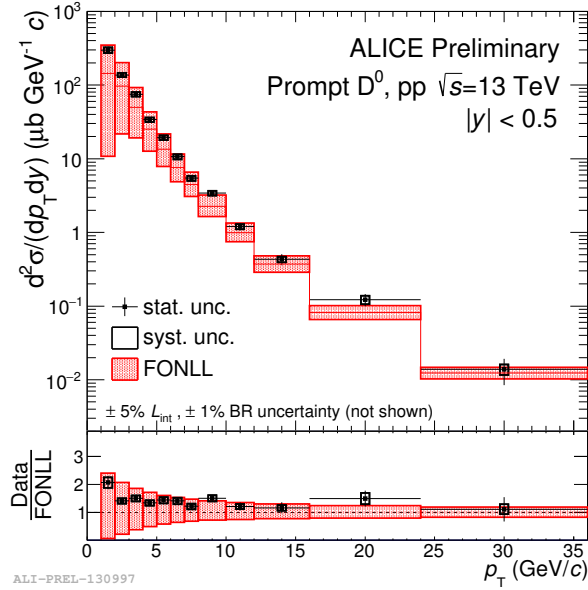


Figure 3.2: p_T -differential production cross section of prompt D^0 measured by ALICE in pp collisions at $\sqrt{s} = 13 \text{ TeV}$ compared to FONLL prediction. Taken from [31].

3.2 D mesons production in Pb-Pb collisions at ALICE at the LHC

The production of open charm mesons D^0 and D^+ at the energy $\sqrt{s_{NN}} = 2.76$ TeV was measured by the ALICE experiment [11]. The chosen decay channels were the same as in the p-p collisions, $D^0 \rightarrow K^-\pi^+$ and $D^+ \rightarrow K^-\pi^+\pi^+$. D^0 and D^+ candidates were reconstructed as a pairs/triplets of right charge particles, that respect following criteria:

- $|\eta| < 0.8$ for daughter particles,
- $p_T > 0.4$ GeV/ c for daughter particles,
- at least 70 associated space points (out of a maximum of 159) in TPC,
- $DCA_d < 250$ μm (D^0),
- $\lambda > 100$ μm (D^0), $\lambda > 120$ μm (D^+),
- $\cos\theta > 0.95$ (D^0), $\cos\theta > 0.99$ (D^+).

In general, the set of cuts for D^+ is more tight because of significantly higher combinatorial background. The PID was the same as in p-p collisions, so by combining the TPC (specific energy loss) and TOF (time of flight) strategies with 3σ cut.

The raw signal was obtained by fitting the invariant mass of pairs/triplets ($M(K\pi)$ for D^0 and $M(K\pi\pi)$ for D^+) with the Gaussian (signal) + exponential (background) function. For low- p_T region of D^0 candidates in centrality class 0-10%, the exponential term was replaced with a fourth-order polynomial function. The invariant mass distributions together with the fit for three different p_T bins are shown in Fig. 3.3. Significance is computed as $S/\sqrt{S+B}$, where S is the bin-counted area of $\pm 3\sigma$ around the mean of the Gaussian and B is the same area of residual background.

The gained raw yield is subsequently corrected with several factors, such as the correction factor for D mesons coming from the weak decay of B hadrons, the branching ratio, the acceptance and the efficiency of the detector, the transverse momentum interval width and the number of analyzed events. Finally one can obtain the invariant yield for different p_T bins. The spectrum for the Pb-Pb collisions in the centrality class 0-10% is shown in Fig. 3.4.

Finally, the nuclear modification factor R_{AA} is shown in Fig. 3.5 for prompt D^0 and D^+ together with D^{*+} for two centrality classes, 0-10% and 30-50%. Within the statistical uncertainty, the results are compatible for all listed D mesons.

For 0-10% centrality class, the maximum suppression is for $p_T = 10$ GeV/ c with the $R_{AA} \sim 0.17$, so the production in Pb-Pb collision is suppressed approximately by a factor of 6 with respect to p-p collision. For 30-50% centrality class, the minimum value of R_{AA} is also for $p_T = 10$ GeV/ c , but the value is $R_{AA} \sim 0.3$, so the suppression is of factor of 3. Therefore, the suppression

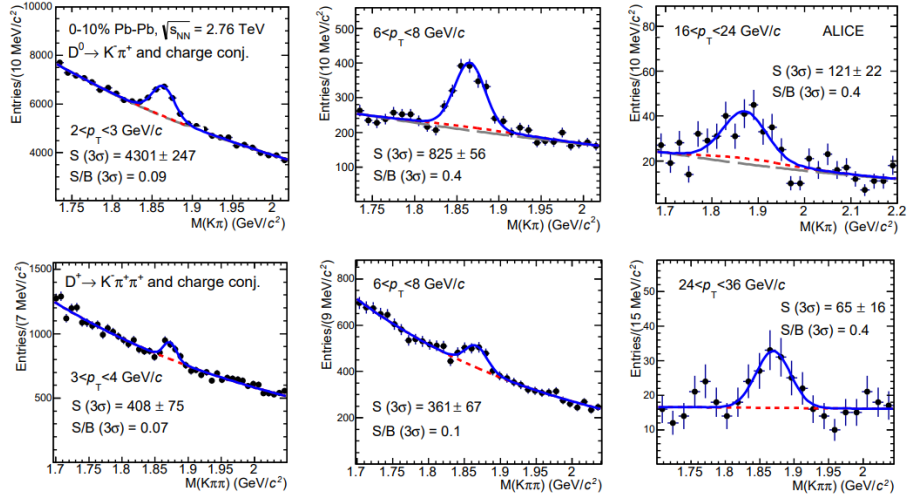


Figure 3.3: Invariant mass distributions for D^0 (top row) and D^+ (bottom row) candidates for three different transverse momentum p_T bins. Taken from [11].

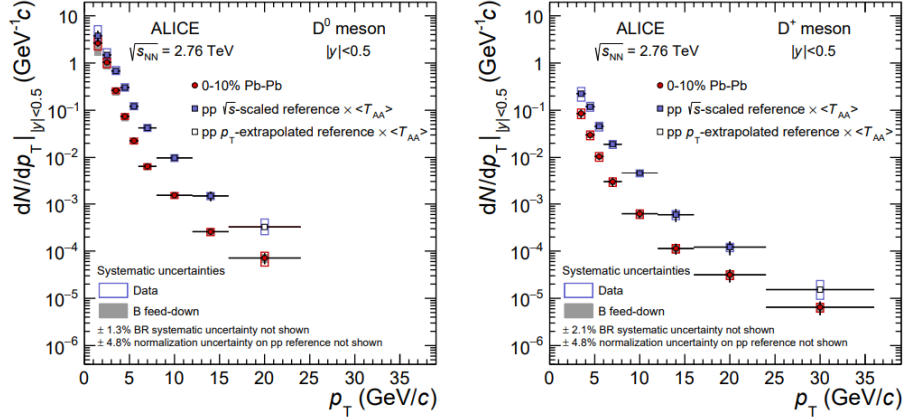


Figure 3.4: Transverse momentum distributions dN/dp_T of prompt D^0 and D^+ in the 0–10% centrality class in Pb–Pb collisions at $\sqrt{s_{NN}} = 2.76$ TeV. Taken from [11].

in high- p_T region is smaller in this centrality class than in the most central collisions.

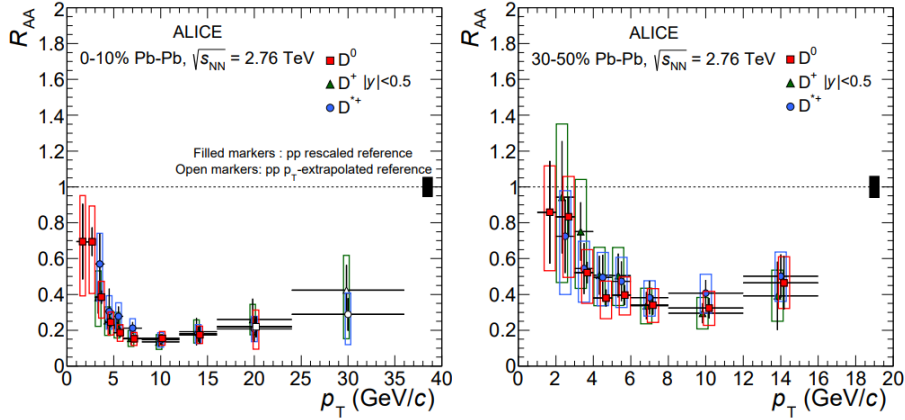


Figure 3.5: Nuclear modification factor of prompt D mesons in the 0–10% (left) and 30-50% (right) centrality class in Pb–Pb collisions at $\sqrt{s_{NN}} = 2.76$ TeV. Taken from [11].

3.3 D mesons production in Au-Au collisions at STAR at the RHIC

The measurement of the production of D mesons was performed at the STAR experiment in Au-Au collisions at $\sqrt{s_{NN}} = 200$ GeV. The analysis of those particles is possible thanks to the HFT detector which is crucial in the secondary vertex measurement and therefore significantly reduces the combinatorial background.

The production of D^0 from [32] is based on ~ 875 M minimum bias events. For the reconstruction, the following set of cuts was used:

- $|\eta| < 1$ for daughter particles,
- $p_T > 0.4$ GeV/ c for daughter particles,
- at least 20 associated space points (out of a maximum of 45) in TPC,
- at least one hit in every layer of PXL and IST,
- π PID:
 - $|n\sigma| < 3.0$ (based on dE/dx from TPC),
 - if TOF is available: $|\frac{1}{\beta} - \frac{1}{\beta_{exp}}| < 0.03$,
- K PID:
 - $|n\sigma| < 2.0$ (based on dE/dx from TPC),
 - if TOF is available: $|\frac{1}{\beta} - \frac{1}{\beta_{exp}}| < 0.03$,

The topological cuts on 5 variables were optimized using the Toolkit for Multivariate Data Analysis (TMVA). These variables were

- decay length λ ,
- distance of closest approach (DCA) between two daughter tracks,
- DCA between the reconstructed track of D^0 and primary vertex (PV),
- DCA between the π track and PV,
- DCA between the K track and PV.

Optimization was independent for 5 different centrality classes (0-10, 10-20, 20-40, 40-60 and 60-80%) and for different D^0 p_T (0-0.5, 0.5-1, 1-2, 2-3, 3-5, 5-8 GeV/c). In addition, the cut $\cos\theta > 0.95$ was used for each combination of centrality class and p_T .

With similar methods as at ALICE experiment (e.g. corrections on efficiency), it is possible to obtain the invariant yield spectrum as a function of p_T . For D^0 in different centrality classes, the transverse momentum distribution d^2N/dp_T is shown in Fig. 3.6. Lines depict fits by Levy function

$$\frac{d^2N}{2\pi p_T dp_T dy} = \frac{1}{2\pi} \frac{dN}{dy} \frac{(n-1)(n-2)}{nT(nT + m_0(n-2))} \left(1 + \frac{\sqrt{p_T^2 + m_0^2} - m_0}{nT}\right)^{-n}, \quad (3.2)$$

where m_0 is the mass of D^0 and n, T and dN/dy are free parameters.

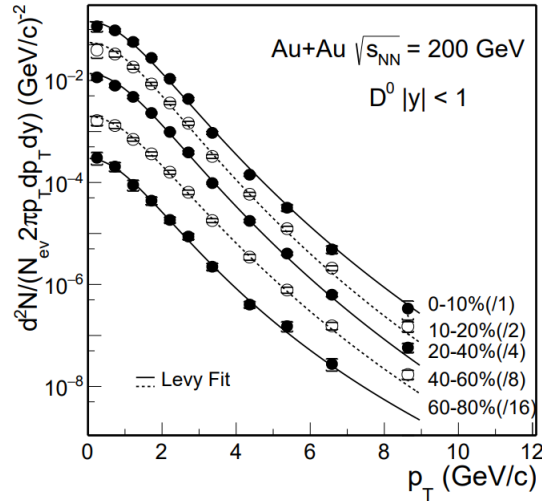


Figure 3.6: Transverse momentum distributions d^2N/dp_T of D^0 for different centrality classes in Au-Au collisions at $\sqrt{s_{NN}} = 200$ GeV. Lines depict Levy function fits. Taken from [32].

To obtain R_{AA} , the STAR Run 9 p-p results were used as a reference. The results are shown in Fig. 3.7 for three different centrality classes - 0-10%, 10-40%, 40-80% for two different data taking campaigns on RHIC: Run14 and Run10/11. Shown results are within the uncertainty with the good accordance with ALICE results shown in Fig. 3.5 - the maximum suppression (by a factor of 5-6 for 10% of the most central collisions) is for $p_T = 10$ GeV/ c . In general we can also conclude that the suppression in the particle production increases towards more central collisions.

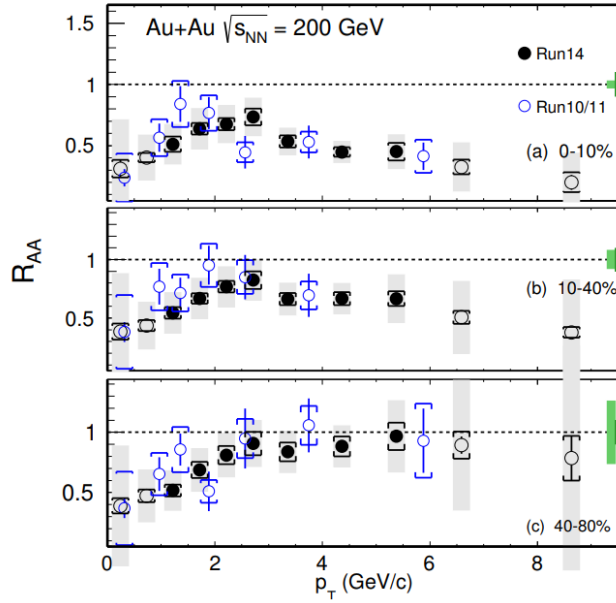


Figure 3.7: Nuclear modification factor R_{AA} of D^0 in the 0–10% (top), 10-40% (center) and 40-80% (bottom) centrality class in Au-Au collisions at $\sqrt{s_{NN}} = 200$ GeV. Taken from [32].

For the D^+ reconstruction, the following topological criteria were used [33]:

- $DCA_d < 80 \mu\text{m}$, where DCA_d is the maximal distance between pairs of decay products,
- $30 \mu\text{m} < \lambda < 2000 \mu\text{m}$,
- $\cos \theta > 0.998$,
- $DCA_\pi < 100 \mu\text{m}$, where DCA_π means the distance of closest approach of the π trajectory to the PV,
- $DCA_K < 100 \mu\text{m}$,

- $\Delta_m < 200 \mu\text{m}$, where Δ_m is the largest side of the triangle $V_{K\pi}V_{K\pi}V_{\pi\pi}$, where the point V_{XY} is situated in the middle of the connection of trajectories of X and Y particles in the point of closest approach.

Raw yield is shown in Fig. 3.8 for the 10% most central Au-Au collisions at $\sqrt{s_{\text{NN}}} = 200 \text{ GeV}$ for two different p_{T} bins. The D^\pm meson is reconstructed using the hadronic channel $D^+ \rightarrow K^-\pi^+\pi^+$. Therefore the background is obtained as the wrong sign combinations (6 different combinations of the $K\pi\pi$ triplet), and the correct sign combinations (2 different combinations for D^+ and its antiparticle, D^-) are for signal pairs, composed from both background and the real signal.

Nuclear modification factor R_{AA} of D^\pm is shown in Fig. 3.9 together with the R_{AA} of D^0 . Within the systematic uncertainty, R_{AA} for both particle is in good accordance.

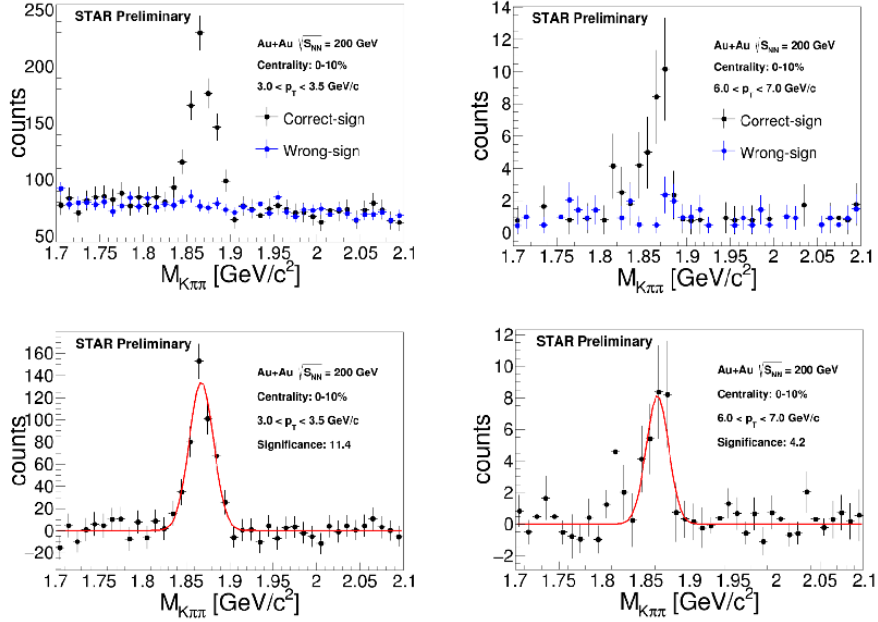


Figure 3.8: Raw yield of D^\pm meson from the hadronic channel $D^+ \rightarrow K^-\pi^+\pi^+$ from the 10% most central Au-Au collisions at $\sqrt{s_{\text{NN}}} = 200 \text{ GeV}$. Taken from [33].

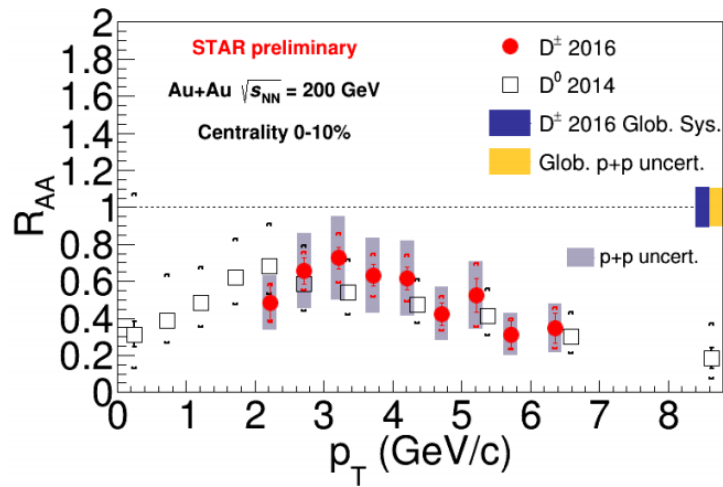


Figure 3.9: Nuclear modification factor R_{AA} of D^\pm in the 0–10% centrality class in Au-Au collisions at $\sqrt{s_{NN}} = 200$ GeV. Taken from [34].

Chapter 4

Reconstruction of D^+ meson in Au-Au collisions with STAR using TMVA

Toolkit for Multivariate Data Analysis (TMVA) is a package implemented in the scientific software framework ROOT that uses machine learning methods to improve all kinds of analysis. In following chapter, the method chosen for D^\pm meson reconstruction, decision trees improved with the boosting, will be explained together with the basic concept of the machine learning itself. Finally, the method will be used on the experimental data from Au-Au collisions at the STAR experiment at the energy per nucleon pair $\sqrt{s_{NN}} = 200$ GeV, in order to reconstruct the D^\pm meson with the significance as high as possible.

4.1 Machine learning in particle physics

Let's have a d dimensional space, where every dimension stands for a variable that we want to use in the analysis (p_T, DCA_d, \dots). Our goal is to make a response function $f : \mathbb{R}^d \rightarrow \mathbb{R}^N$, where $\vec{x} \in \mathbb{R}^d$ is a vector of input set of variables and $\vec{y} \in \mathbb{R}^N$ is a vector of output. The output changes based on the type of algorithm used.

In the ideal case, $N \ll d$, therefore one can simplify the problem. The classification problem we are dealing with is the determination whether inputs \vec{x} are background-like or signal-like. Therefore it is a binary classification problem, so we set $N = 1$. Our output y is a number between -1 (pure background) and 1 (pure signal). This kind of problem is part of the supervised machine learning, thus the training part is proceeded with known input and output as well. On the other hand, in the unsupervised machine learning case, one knows the input, but the output is unknown, therefore the result is a connection between input variables.

There are several methods how to obtain the response function. The basic one is the optimization of the rectangular cuts which is the classical approach in the high-energy physics. In several problems, such as D^+ reconstruction, the classical approach is not sufficient (mostly in low p_T region) as there is much larger number of combinatorial background present. Only one hypercube is chosen from the phase space \mathbb{R}^d , usually the one with the best signal-to-background ratio. The rectangular cuts optimization is a method which suffers on the curse of dimensionality, therefore it is really important to chose wisely the set of variables used for the training and use only those with the high discriminating potential.

The method that is very popular in the high-energy physics is the classification with the use of boosted decision trees. A binary decision tree, shown in the Fig. 4.1, has the whole sampe (signal and background) in the root note. Data are subsequently divided into two disjoint sets based on a value of one single variable. In the following step, another division is occurring, either with the different discriminating variable, or with the same, but with the different cutting value. The leaf nodes, labeled S for the signal and B for the background, get the label based on the majority of data that end within this node in the training part.

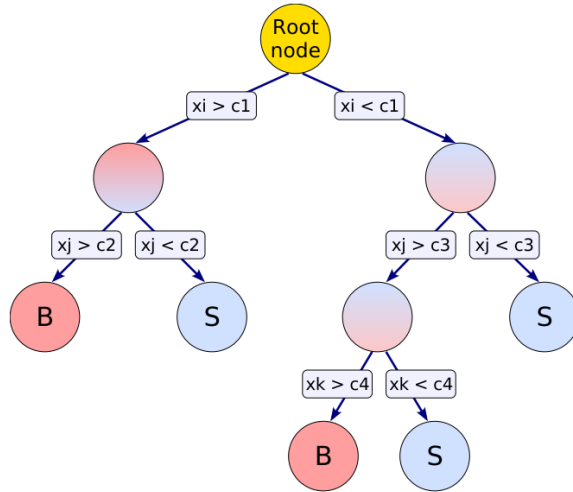


Figure 4.1: Schematic representation of a decision tree. Taken from [35].

There is indeed a similarity between the decision tree and the rectangular cuts method, the advantage of the former is that the phase is divided into large number of hypercubes and each is individually assigned either as signal-like or as background-like whereas the rectangular cuts method uses only one hypercube from the whole phase space. Maximum depth of a decision tree is a maximum number of separation from a leaf to the root, in the example in Fig. 4.1 it is

three.

The statistical fluctuations in the training sample can cause a large instability of the decision tree, which is undoubtedly one of the main disadvantage of using the algorithm. Adding the boosting, thus using a forest of trees instead of a single tree, can fix this instability. All the trees are trained using the same sample. The final value of the response function is gained as a weighted sum over each tree, the weights are obtained after several iterations, where only incorrectly classified events are used for the next step. Boosted decision trees are a powerful tool, stable with respect to the statistical fluctuations and with a high separation power. When trees are shallow, so the maximum depth of a tree is limited, the probability of overtraining is highly reduced.

4.2 Training phase

To train the algorithm and to obtain the good performance, we need a signal and background sample, and tuning the algorithm itself. Before doing those steps, one need to choose the set of variables that will be using in the analysis. Following section will be subdivided accordingly based on the steps done during the training phase. At the end, the output of the TMVA training phase will be shown.

4.2.1 Discriminating variables

The choice of variables for the machine learning based analysis of D^\pm was influenced by the classical analysis. Summary of rectangular cuts used in the standard analysis in D^\pm hadronic decay channel $D^+ \rightarrow K^- \pi^+ \pi^+$ with the STAR experiment in Au-Au collisions at $\sqrt{s_{NN}} = 200$ GeV is in Tab. 4.1.

As it was already mentioned in the previous chapter, decay length λ is the distance between the primary and secondary vertex, the pointing angle θ is the angle between the vector sum of momenta of the triplet and the decay length vector. The maximal reconstructed vertex pair distance Δ_m is shown in Fig. 4.2 together with the maximal DCA between $\pi\pi$, πK , $K\pi$, as DCA_d .

At first, the training was made with 7 variables:

- $3 \times$ DCA of a decay product (K, π, π) to the primary vertex,
- maximal DCA between $\pi\pi, \pi K, K\pi$ DCA_d ,
- pointing angle $\cos \theta$,
- decay length λ ,
- maximal reconstructed vertex pair distance Δ_m .

Since the Δ_m was highly correlated with the decay length λ ($\sim 90\%$ for both signal and background), we decided to exclude this variable from the analysis. Although BDT are not affected by the correlation between variables, other

Event selection	Vertex position in beam direction	$ v_z < 6$
	Correlation between VPD and TPC	$ v_z(VPD) - v_z < 3$
Track selection	Hits in HFT	PXL1, PXL2, IST
	Hits in TPC	$N_{TPC} > 20$
Topological Cuts	DCA between $\pi\pi, \pi K, K\pi$	$DCA_d < 80 \mu\text{m}$
	D^\pm decay length	$30 \mu\text{m} < \lambda < 2000 \mu\text{m}$
	Pointing angle	$\cos\theta > 0.998$
	Max reconstructed vertex pair distance	$\Delta_{max} < 200 \mu\text{m}$
	Daughter DCA to primary vertex	$DCA_{\pi 0} > 100 \mu\text{m}$ $DCA_{K 0} > 80 \mu\text{m}$
Particle identification	TPC particle transverse momentum	$p_T^\pi > 0.5 \text{ GeV}/c$
		$p_T^K > 0.5 \text{ GeV}/c$
	TPC ionization loss standard deviation	$n\sigma_\pi < 3$
		$n\sigma_K < 2$
	TOF inverse velocity	$ \frac{1}{\beta} - \frac{1}{\beta_\pi} < 0.03$
$ \frac{1}{\beta} - \frac{1}{\beta_K} < 0.03$		

Table 4.1: Summary of standard rectangular cuts used for D^\pm analysis on STAR experiment. Taken from [33].

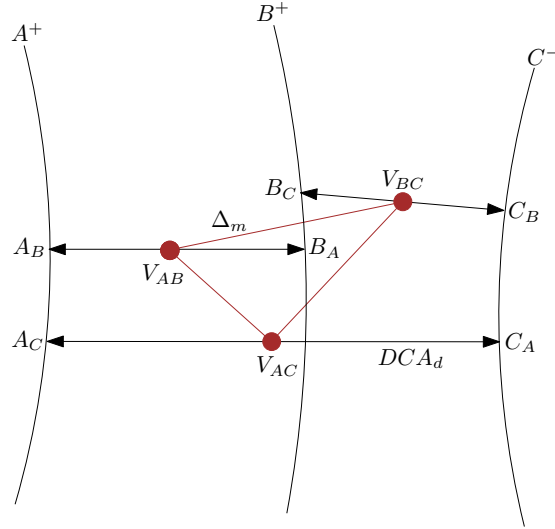


Figure 4.2: Scheme of a particle triplet.

methods, such as rectangular cuts optimization or maximum likelihood method, can be significantly influenced by it. Considering the usage of those method in the future, it is convenient to use just the first six itemized variables for this analysis.

4.2.2 Signal and background sample production

As a signal sample for the training phase, 8.366 M D^\pm mesons were produced in the data-driven simulator. The meson is created and decayed in PYTHIA through the hadron channel $D^+ \rightarrow K^- \pi^+ \pi^+$. The kinematical variables (mostly p_T and DCA) of decay products, triplets $K\pi\pi$ with the right sign combination, were smeared in the detector using its effectivity and acceptance extracted from data from HFT, TPC and TOF from Run14, thus the smeared simulation will be consistent with the data from Au-Au collisions at the STAR experiment.

While the smearing of the transverse momentum p_T is basically impossible to observe on the distribution shown in Fig. 4.3 (left), the distribution of the distance of closest approach of decay products from the simulated decay is very different from the smeared one. The latter is shown in Fig. 4.3 (right), the significant peak around 30 μm is caused by the resolution of HFT, shown in Fig. 2.5, which converges towards 20 μm .

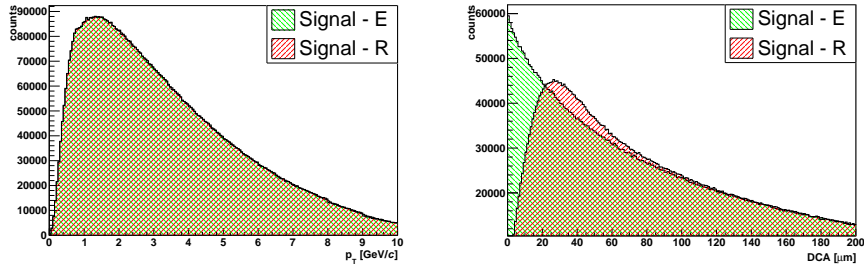


Figure 4.3: Distribution of transverse momentum p_T (left) and DCA (right) of kaons from the simulation of D^\pm decay. E (green) is for the exact value while R (red) is for reconstructed, so for the smeared value.

The background sample is $K\pi\pi$ triplets from data collected by the STAR experiment during the Run 14 with excluding the right sign combinations ($K^- \pi^+ \pi^+$ and $K^+ \pi^- \pi^-$). The data is from Au-Au collisions at the energy per nucleon pair $\sqrt{s_{NN}} = 200$ GeV. With the rectangular cuts significantly looser than for classical analysis (Tab. 4.1), e.g. $p_T > 0.2$ GeV/ c , $DCA > 20$ μm , $\cos\theta > 0.95$, we obtained in total 8.414 M triplets.

Distributions of all the TMVA input variables, namely DCA for kaon and two pions, DCA_d , $\cos\theta$ and λ , for signal (blue) and background (red) for D^\pm candidate in the p_T range 2–2.5 GeV/ c are shown in Fig. 4.4. For this p_T range and cuts $p_T > 0.4$ GeV/ c , DCA of decay products > 20 μm and $\cos\theta > 0.95$, we obtain 41k triplets in the signal sample and 436k in the background sample.

The training was made separately for 11 triplet p_T bins in the range from 0 to 6 GeV/ c (0-1, 1-1.5, 1.5-2, ..., 5.5-6 GeV/ c) and for 4 different event centrality classes (0-10%, 10-40%, 40-80% and the whole range, 0-80%).

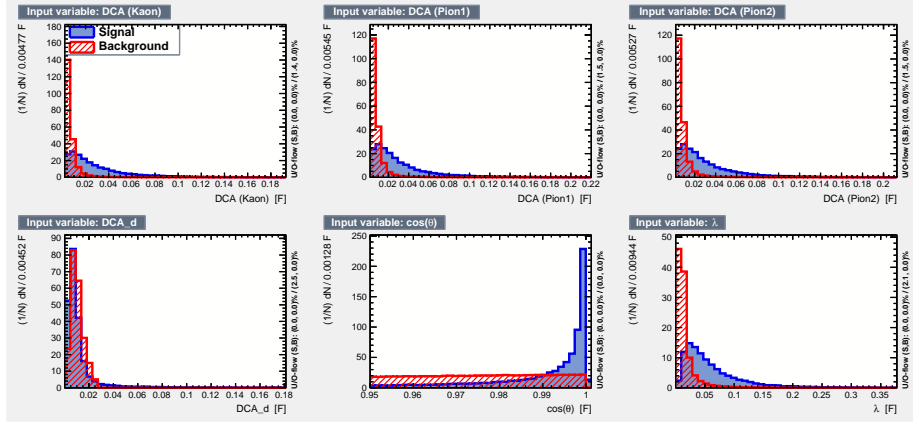


Figure 4.4: Distributions of input variables within the TMVA for the D^\pm candidate p_T range 2 – 2.5 GeV/ c .

4.2.3 BDT setup

The setup of the Boosted Decision Tree method used for all p_T and centrality bins is the same. During the training phase, 850 trees with the maximum depth of three were produced. The boosting chosen within the TMVA is adaptive boost (AdaBoost). This algorithm is optimized to have the best performance while combining a lot of weak classifiers. During the training with the AdaBoost, misclassified triplets from a decision tree obtain higher weight before the training of the following tree occurs [35].

4.2.4 Training output

As was mentioned in one of the previous sections, the training was made separately for 11 triplet p_T bins for 4 different centrality classes (44 unique combinations). The TMVA package provides graphical output from the training part.

For D^\pm candidate in the p_T range 2 – 2.5 GeV/ c in 0-10% most central collisions, the linear correlation matrices for the signal and the background are shown in Fig. 4.5. For the signal, DCA_d and λ are slightly correlated with other variables (except the $\cos\theta$). All variables in the background sample are uncorrelated.

Another important check after the training phase is the overtraining one, even though BDT is one of the method proved to be very resistant to this. The half of data from both signal and background sample is used for the training. Subsequently, when we have 850 decision trees and the algorithm is trained, the second half of the data is evaluated on the created trees. During this evaluation, we still know either the data is the signal or the background, so we can compare the BDT response function for the training and the testing sample. The output

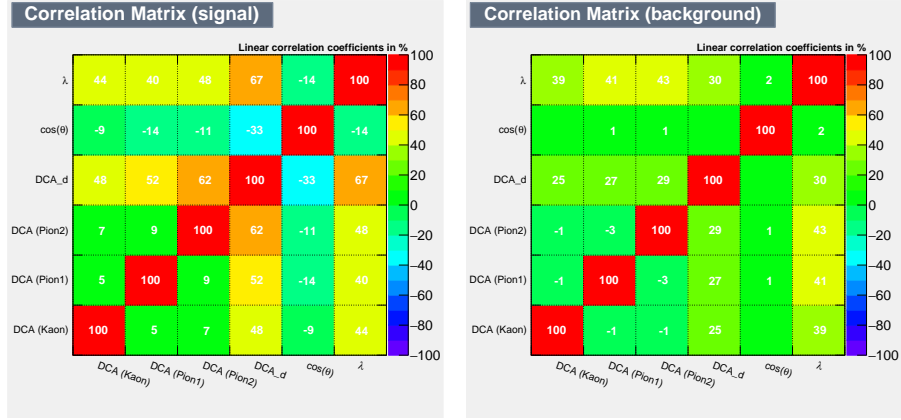


Figure 4.5: Linear correlation matrices for signal (left) and background (right) from the training of TMVA for D^\pm analysis in the p_T range 2 – 2.5 GeV/c from 0-10% most central collisions.

for the training of TMVA for the D^\pm analysis in the p_T range 2 – 2.5 GeV/c, shown in the Fig. 4.6, is consistent for both training and testing samples.

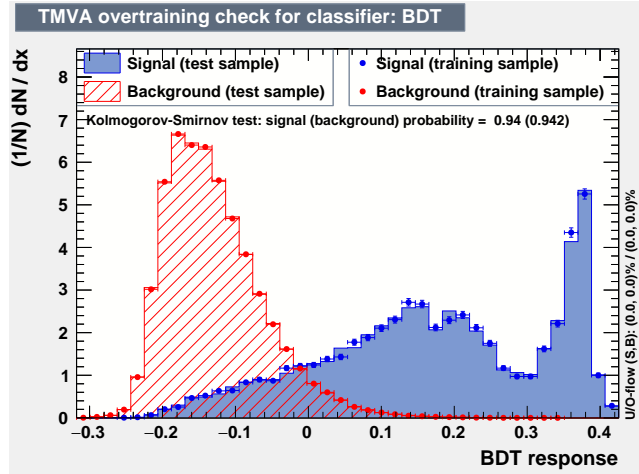


Figure 4.6: Overtraining check from the TMVA training phase for the D^\pm analysis in the p_T range 2 – 2.5 GeV/c.

In the application part, we need to choose the cut on the BDT response function. Within the TMVA, for every trained method we obtain a classifier cut efficiency plot, from which we can deduce the optimal cut value - for this analysis, we decided to use the maximum significance S ($S = N_s/\sqrt{N_s+N_b}$, where N_s and N_b are number of signal and background pairs, respectively). However, to obtain the significance as a function of the BDT response function, we need

to predict a ratio between the signal and the background in the real data (when we do not know whether the candidate is signal or not). In other words, we need to predict how many D^\pm mesons can we found in a sample with a fixed number of entries.

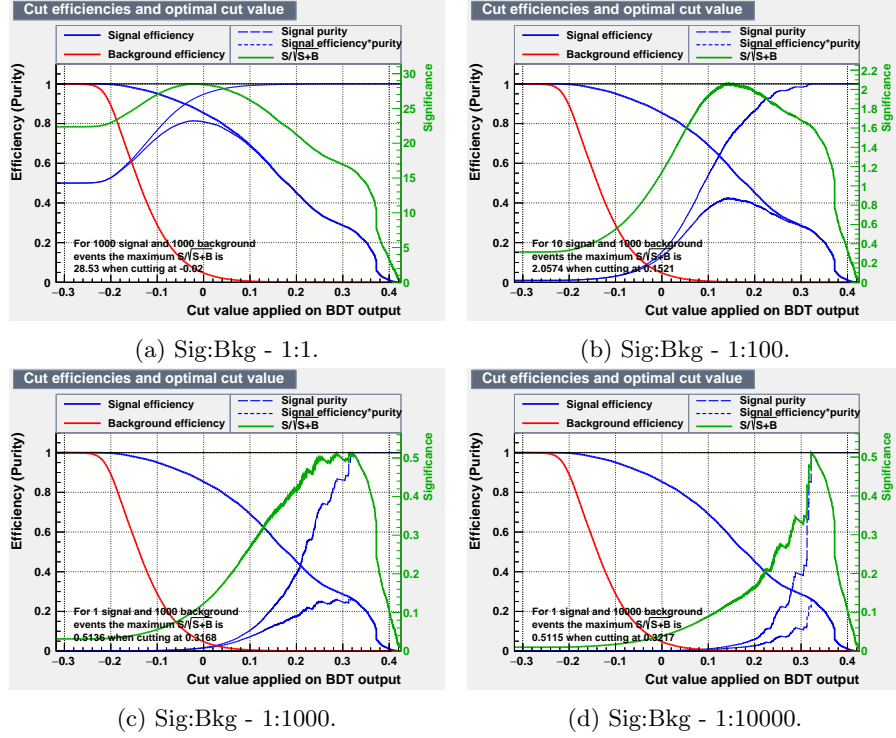


Figure 4.7: Cut efficiencies and optimal cut value plots from the training of TMVA for D^\pm analysis in the p_T range 2 – 2.5 GeV/c for different ratios of signal and background.

Cut efficiency plot for different ratios of signal and background are shown in Fig. 4.7. The significance, the value which we are interested in, is plotted in green. One can observe that the optimal cut value significantly differs for displayed signal to background ratios.

There are several methods how to choose the optimal ratio without blindly guessing. The first deduces the ratio from the analysis of D^0 . However, this method is strongly biased, since one has to rely on the result of another analysis. Because of this reason, we choose the method in which we deduce the optimal cut in the application phase.

4.3 Application phase and results

The data we used for the D^\pm analysis are from the STAR experiment Run14 from the Au-Au collisions at the energy $\sqrt{s_{NN}} = 200$ GeV. We produced the root files necessary for the analysis from the picoDst with the $p_T > 0.4$ GeV/ c , $DCA > 20$ μm and $\cos\theta > 0.95$, the same criteria as the preselection cuts inside the TMVA classification algorithm for the training.

The BDT trained algorithm was applied on data and we saved BDT response for every triplet, separately based on the sign combination (the right sign combination for the D^\pm candidate and the wrong sign combination for the background). Subsequently, we produced histograms of the mass of the $K\pi\pi$ triplet (so of the D^\pm candidate) based on the BDT cut - we accepted only the candidate with the BDT response function bigger than the selected cut value. Number of histograms changed for different p_T bins and centrality classes, but it has always started with the BDT cut at 0 with the step of 0.025. Based on the combination of p_T and the centrality, the BDT cut for the last histogram produced varied between 0.275 and 0.4.

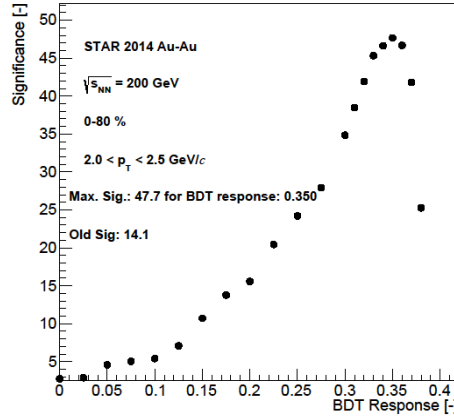


Figure 4.8: Significance as a function of the BDT cut for the D^\pm analysis in the p_T range 2 – 2.5 GeV/ c for the 0-80% centrality.

To obtain the significance, we need to subtract the background first to obtain the raw yield. At the beginning, we need to normalize both histogram with mass of the triplet. This was done by bin-counting the region 3σ outside the peak of both correct and wrong sign combination and subsequently scaling the wrong sign histograms. As a following step, the scaled background was subtracted and each histogram with the right sign combination was fitted with the Gaussian + polynomial function. For each bin, the value computed from the polynomial part of the function was subtracted and finally, we obtained the raw yield and we were able to compute the significance. The dependence of the significance on the BDT cut for the p_T range 2 – 2.5 GeV/ c and the 0-80% centrality is shown

in Fig. 4.8.

For the p_T range with sufficient statistics (1-5 GeV/ c), we obtain a smooth dependence of the significance on the BDT cut. For higher p_T regions, the lack of statistics in the training phase may cause fluctuation in the significance plot.

Once we had the graph of significance and we knew the region of BDT cut with the maximum significance, we changed the step from 0.025 to a significantly smoother one, so to 0.01 in the region (as is already shown in Fig. 4.8).

The improvement of the significance changes for every p_T bin and for every centrality class. For centrality 0-10% and p_T range of D^\pm candidate 2.5-3 GeV/ c , the significance improves from 11.0 (classical approach) to 16.4 (analysis with the usage of the machine learning), as is shown on the invariant mass plots for both approaches in Fig. 4.9. The significance of the latter is 1.5 times larger than of the former one.

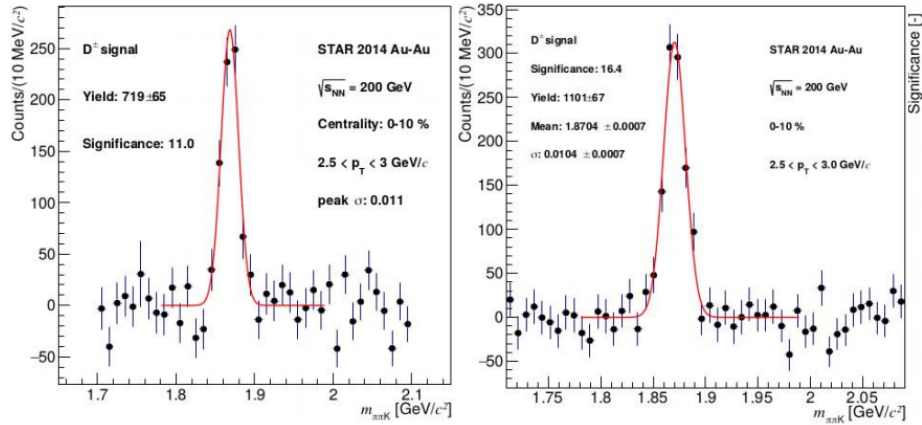


Figure 4.9: Invariant mass of $K\pi\pi$ triplet for centrality 0-10% and p_T range of D^\pm candidate 2.5-3 GeV/ c for the classical (left) and TMVA analysis (right).

Lower the p_T region, more combinatorial background occurs, therefore the usage of multivariate data analysis is becoming more and more important, as it can be seen in Fig. 4.10, where is shown the invariant mass of the $K\pi\pi$ triplet for centrality 0-10% and p_T range of D^\pm candidate 2-2.5 GeV/ c . The invariant mass from the classical analysis based on rectangular cuts summarized in the Tab. 4.1 is shown on left with the significance of 4.1. With the use of BDT, we obtain the significance of 19.7, which is 4.8 times more than the previous case.

Summary of significances for different p_T bins of D^\pm meson in the range 2.0 - 5.0 GeV/ c for classical approach analysis (rectangular cuts) and for analysis with the use of boosted decision trees is in Tab. 4.2. The comparison is also shown in Fig. 4.11.

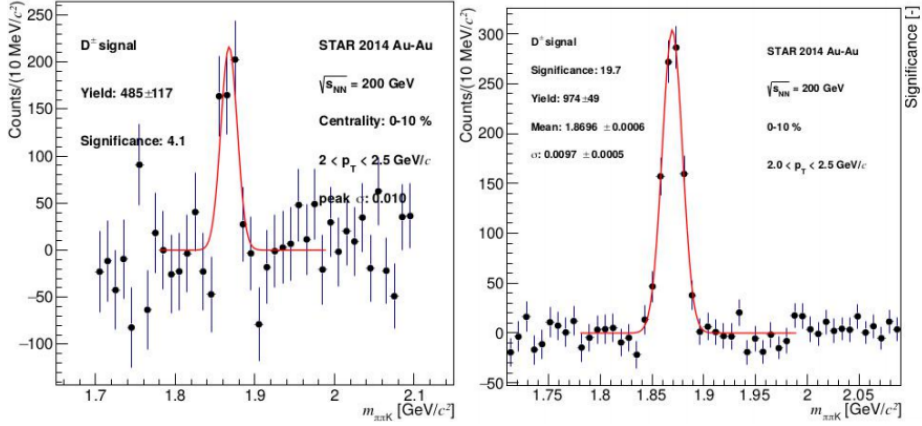


Figure 4.10: Invariant mass of $K\pi\pi$ triplet for centrality 0-10% and p_T range of D^\pm candidate 2-2.5 GeV/c for the classical (left) and TMVA analysis (right).

p_T range [GeV/c]	significance of cuts	significance of BDT	ratio BDT/cuts
2.0 - 2.5	4.1	19.7	4.8
2.5 - 3.0	11.0	16.4	1.5
3.0 - 3.5	12.5	17.1	1.4
3.5 - 4.0	12.1	16.5	1.4
4.0 - 4.5	9.9	13.8	1.4
4.5 - 5.0	6.9	8.8	1.3

Table 4.2: Summary of obtained significance for different p_T bins of D^\pm meson in 0-10% event centrality for classical approach analysis (rectangular cuts) and for analysis with the use of boosted decision trees.

4.4 Systematic uncertainties

When performing the classical analysis with the use of rectangular cuts, the systematic uncertainties are usually obtained by varying topological cuts. The yield from D^\pm reconstruction from Au-Au collisions at $\sqrt{s_{\text{NN}}} = 200 \text{ GeV}/c$ from STAR Run 14 has systematic uncertainty from changing single cut in a time, this variation was made individually for each p_T bin and centrality class.

The relative systematic uncertainty for 0-80% centrality class in all p_T bins above 2 GeV/c is slowly rising from 9.2% (for p_T of D^\pm 2-2.5 GeV/c) to 10.3% (for p_T of D^\pm 5.5-6 GeV/c). For p_T 1-2 GeV/c , this uncertainty is 50%. For 10% of the most central collisions, the uncertainty is bigger, varying from 14.9 for 2-2.5 GeV/c to 18.6 for 5.5-6 GeV/c [33].

Another factor that needs to be included in the systematic uncertainties is the efficiency and the geometrical acceptance of the STAR detector, which includes all used detectors (HFT, TPC, TOF). The overall systematic uncertainty of 5% was gained from the data-driven simulators.

Last considered uncertainty in the classical approach is the uncertainty of

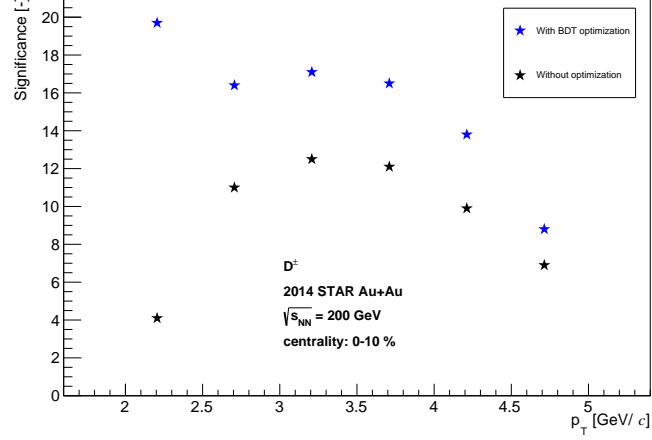


Figure 4.11: Obtained significance for different p_T bins of D^\pm meson in 0-10% event centrality for classical approach analysis (rectangular cuts) and for analysis with the use of boosted decision trees.

the branching ratio which is for hadronic channel $D^+ \rightarrow K^- \pi^+ \pi^+$ $BR = (9.13 \pm 0.19)\%$ with the uncertainty 2.1%.

Using the multivariate data analysis, the BDT cut can be treated as a regular cut. Then the systematic uncertainty is obtain by varying the cut value, what we have done while looking for the optimal cut value for obtaining the best significance. Another possibility is to retrain BDTs with a different number of trees and a different maximum depth of a tree, or changing a boosting algorithm.

Summary

The main goal of this work was to improve the D^\pm meson reconstruction with use of Boosted Decision Trees machine learning method. The study of charmed mesons is important, since heavy quarks can probe the quark-gluon plasma. An overview of charmed mesons measurement in heavy-ion collisions was introduced.

The reconstruction of D^\pm meson in this thesis is made from Run 14 Au-Au collisions measured by the STAR experiment at the energy per nucleon pair $\sqrt{s_{NN}} = 200$ GeV/ c . It is possible with the classical approach using rectangular cuts on variables, an improvement can be made with TMVA package implemented within the ROOT framework. In the chapter dedicated to the analysis, the BDT setup is described together with the choice of discriminating variables and the production of signal and background sample used. Raw yields of D^\pm meson were obtained separately for different transverse momentum and event centrality classes. The significance was improved $1.3 - 4.8 \times$ compared to the classical approach based on transverse momentum bin of D^\pm meson. Finally, systematic uncertainties were discussed.

Obtained results will be used for the computation of nuclear modification factor R_{AA} of D^\pm meson in Au-Au collisions once the effectivity and systematic uncertainty are obtained. The multivariate data analysis is important mostly in the region of lower transverse momentum of the D^\pm meson because of large combinatorial background. Concerning the region of high transverse momentum of the D^\pm meson, the optimization of BDT setup has to be done, since in this region the amount of data in training sample is not sufficient for current BDT setup.

The results of this work, a considerable improvement of the significance of D^\pm meson, were presented at the STAR Collaboration meeting at Lehigh University, Pennsylvania, USA, in July 2018.

Bibliography

- [1] M. Tanabashi et al. *The Review of Particle Physics*. Phys. Rev. D 98, C38, 2018.
- [2] R. Vogt. *Ultrarelativistic Heavy-Ion Collisions*. Elsevier, 2007. ISBN 978-0-444-52196-5.
- [3] R. Pasechnik and M. Šumbera. *Phenomenological Review on Quark-Gluon Plasma: Concepts vs. Observations*. Universe 2017, 3, 7.
- [4] D. McDonald. *Overview of results from phase I of the Beam Energy Scan program at RHIC*. EPJ Web Conf., 95:01009, 2015.
- [5] J. F. Grosse-Oetringhaus. *CERN Summer Student Lectures 2018: Introduction to Heavy-Ion Physics*. 2018.
- [6] P. Rosnet. *Quark-Gluon Plasma: from accelerator experiments to early Universe*. 2015. arXiv:1510.04200.
- [7] T. Lenzi. *Development and Study of Different Muon Track Reconstruction Algorithms for the Level-1 Trigger for the CMS Muon Upgrade with GEM Detectors*. 2013. arXiv:1306.0858.
- [8] R. Snellings. *Elliptic Flow: A Brief Review*. New J. Phys., 13:055008, 2011.
- [9] S. Sarkar, H. Satz, and B. Sinha. *The Physics of the Quark-Gluon Plasma: Introductory Lectures*. Springer Berlin Heidelberg, 2009. ISBN 978-3-642-02286-9.
- [10] L. Kramárik. *Measurements of D^0 production in $d+Au$ collisions at $\sqrt{s_{NN}} = 200$ GeV by the STAR experiment*. Quark Matter Conference, 2018.
- [11] J. Adam et al. *Transverse momentum dependence of D -meson production in $Pb-Pb$ collisions at $\sqrt{s_{NN}} = 2.76$ TeV*. JHEP, 03:081, 2016.
- [12] BNL. *Brookhaven National Laboratory*. <https://www.bnl.gov>. Online, accessed 14 April 2018.
- [13] Nobelprize.org. *The official web site of the Nobel Prize*. <https://www.nobelprize.org/>. Online, accessed 14 April 2018.

- [14] J. Alessi. *Electron Beam Ion Source (EBIS) pre-injector project - Conceptual Design Report*. 2005. BNL-73700-2005-IR.
- [15] M. Okamura and T. Kaneshue. *Commissioning of the Laser Ion Source for RHIC EBIS*. RIKEN Accel. Prog. Rep, 48, 2015.
- [16] E. Beebe, J. Alessi, et al. *Reliable operation of the Brookhaven EBIS for highly charged ion production for RHIC and NSRL*. 2014. BNL-105887-2014-CP.
- [17] W. Wong and Y. Y. Lee. *Design and construction status of the AGS Booster accelerator*. 1988. BNL-41030.
- [18] W. W. Mackay et al. *AGS to RHIC transfer line: Design and commissioning*. <http://www.rhichome.bnl.gov/RHIC/Runs/RhicAtr.pdf>, 1996. Online, accessed 20 April 2018.
- [19] W. Fischer. *Run overview of the Relativistic Heavy Ion Collider*. <http://www.agsrhichome.bnl.gov/RHIC/Runs/>, 2018. Online, accessed 13 August 2018.
- [20] I. Alekseev et al. *Configuration Manual Polarized Proton Collider at RHIC*. <https://www.bnl.gov/cad/accelerator/docs/pdf/RHICPPCMan.pdf>. Online, accessed 15 April 2018.
- [21] BNL. *The STAR experiment*. <https://www.star.bnl.gov>. Online, accessed 14 April 2018.
- [22] PHENIX Collaboration. *sPHENIX: An Upgrade Proposal from the PHENIX Collaboration*. 2014. arXiv:1501.06197.
- [23] S. Radhakrishnan. *Measurements of open charm and bottom production in 200 GeV Au+Au collisions with the STAR experiment at RHIC*. Quark Matter Conference, 2018.
- [24] STAR Collaboration. *STAR Project Conceptual Design Report Update*. <https://www.star.bnl.gov/public/tpc/notebooks/StarCDR.pdf>, 1993. Online, accessed 18 April 2018.
- [25] D. Beavis et al. *The STAR Heavy Flavor Tracker - Technical Design Report*. https://drupal.star.bnl.gov/STAR/system/files/HFT_TDR_Final.doc, 2011. Online, accessed 20 April 2018.
- [26] L. Adamczyk et al. *Measurement of D^0 azimuthal anisotropy at mid-rapidity in Au+Au collisions at $\sqrt{s_{NN}} = 200$ GeV*. 2017. arXiv:1701.06060.
- [27] STAR Collaboration. *The STAR Time Projection Chamber: A Unique Tool for Studying High Multiplicity Events at RHIC*. 2003. arXiv:0301015.

- [28] STAR Collaboration. *Technical Design Report for the iTPC Upgrade*. https://drupal.star.bnl.gov/STAR/files/TDRiTPCUpgrade_final.pdf, 2015. Online, accessed 20 April 2018.
- [29] STAR Collaboration. *Proposal for a Large Area Time of Flight System for STAR*. http://www.star.bnl.gov/~ruanlj/MTDreview2010/TOF_20040524.pdf, 2004. Online, accessed 20 April 2018.
- [30] W.J. Llope et al. *The TOFp/pVPD Time-Of-Flight System for STAR*. Nuclear Instruments and Methods in Physics Research Section A: Accelerators, Spectrometers, Detectors and Associated Equipment, 522(3):252 – 273, 2004.
- [31] J. Hamon. *D-meson production in proton-proton collisions with ALICE at the LHC*. 2018. arXiv:1802.09256.
- [32] X. Chen et al. *Analysis Note: Measurement of D^0 meson production in Au+Au collisions at $\sqrt{s_{NN}} = 200$ GeV*, 2018.
- [33] J. Kvapil. *D^\pm meson production in Au+Au collisions at $\sqrt{s_{NN}} = 200$ GeV measured by the STAR experiment*. Quark Matter Conference, 2017.
- [34] J. Vaněk. *Production of D^\pm Mesons in Au+Au Collisions at $\sqrt{s_{NN}} = 200$ GeV measured by the STAR Experiment*. Quark Matter Conference, 2018.
- [35] A. Hoecker et al. *TMVA 4: Toolkit for Multivariate Data Analysis with ROOT, Users Guide*. 2013. arXiv:0703039.